universität wien

MASTERARBEIT | MASTER'S THESIS

Titel | Title

Analysis of mineral dust during the ACCLIP campaign 2022 in South Korea

verfasst von | submitted by

Mirjam Magdalena Rieser BSc

angestrebter akademischer Grad | in partial fulfilment of the requirements for the degree of

Master of Science (MSc)

Wien | Vienna, 2025

Studienkennzahl lt. Studienblatt | Degree programme code as it appears on the student record sheet:	UA 066 876
Studienrichtung lt. Studienblatt | Degree programme as it appears on the student record sheet:	Masterstudium Physics
Betreut von | Supervisor:	Univ.-Prof. Dr. Bernadett Weinzierl
Mitbetreut von | Co-Supervisor:	Dr. Maximilian Dollner MSc

Abstract

In this study, the characteristics of mineral dust particles, transported from Asian dust sources to the atmosphere are discussed by analyzing a measured mineral dust layer over the main land of South Korea. The aim of this thesis is to discuss the potential source region of this Asian mineral dust layer, characterize its microphysical properties, and determine their potential to act as ice nucleating particle (INP).

Mineral dust is one of the most abundant aerosol particle type in the atmosphere, impacting climate by acting as ice nucleating particles and interacting with radiation. Asian dust makes up 13% of total atmospheric dust but 40% in the upper troposphere and lower stratosphere (UTLS) due to deep convection during the Asian summer monsoon.

The Asian summer monsoon Chemical and CLimate Impact Project (ACCLIP) was an aircraft-based field experiment between July and September 2022, stationed in Osan, South Korea. The main goal was to investigate the transport of gases and aerosol particles emitted in Asia to the global UTLS. The University of Vienna's Cloud, Aerosol, and Precipitation Spectrometer (UNIVIE-CAPS) was one of the instruments, installed on the high-altitude research aircraft WB-57, measuring aerosol particles between 0.5 and 930 µm. During the research flight on August 4th, 2022, a mineral dust layer originating from Mongolia and the north of China was observed over the mainland of South Korea between 7450 m to 7069 m altitude. Compared to background conditions, number concentrations for particles with diameters up to 2.6 µm were enhanced in the mineral dust layer with a maximum for particles with a diameter of 0.6 µm with 4.5 #/cm^3. These values agree with measurements of mineral dust from various field experiments carried out in the past and summarized by Adebiyi et al. (2023). Additionally, the influence of the measured dust layer on the formation of mixed-phase clouds was investigated by deriving the ice nucleation particle (INP) concentration utilizing the parameterization by DeMott et al. (2010). For the observed Asian dust layer, an INP concentration of 0.283 (± 0.051) #/L^{-1} was determined. These values are in agreement with measured INP concentrations during dust events in East Asia.

Kurzfassung

In dieser Studie werden die Eigenschaften von Mineralstaubpartikeln, die aus asiatischen Staubquellen in die Atmosphäre transportiert werden, anhand der Analyse einer gemessenen Mineralstaubschicht über dem Festland von Südkorea diskutiert. Ziel dieser Arbeit ist es, die potenzielle Herkunftsregion dieser asiatischen Mineralstaubschicht zu erörtern, ihre mikrophysikalischen Eigenschaften zu charakterisieren und ihr Potenzial, als Eiskeimpartikel (INP) zu wirken, zu bestimmen.

Mineralstaub gehört zu den häufigsten Aerosolpartikeln in der Atmosphäre und beeinflusst das Klima, indem er als INP wirkt und mit der Strahlung wechselwirkt. Asiatischer Staub macht 13 % des gesamten atmosphärischen Staubs aus, aber 40 % in der oberen Troposphäre und unteren Stratosphäre (UTLS) aufgrund der tiefen Konvektion während des asiatischen Sommermonsuns.

Das Asian summer monsoon Chemical and CLimate Impact Project (ACCLIP) war ein flugzeuggestütztes Feldexperiment zwischen Juli und September 2022, das in Osan, Südkorea, stationiert war. Hauptziel war die Untersuchung des Transports von in Asien emittierten Gasen und Aerosolpartikeln in die globale UTLS. Das „University of Vienna's Cloud, Aerosol, and Precipitation Spectrometer" (UNIVIE-CAPS) war eines der Instrumente, die auf dem Höhenforschungsflugzeug WB-57 installiert wurden und Aerosolpartikel zwischen 0,5 und 930 µm messen. Während des Forschungsfluges am 4. August 2022 wurde eine aus der Mongolei und Nordchina stammende Mineralstaubschicht über dem südkoreanischen Festland zwischen 7450 m und 7069 m Höhe vermessen. Im Vergleich zu den Hintergrundbedingungen waren die Anzahlkonzentrationen für Partikel mit einem Durchmesser von bis zu 2,6 µm in der Mineralstaubschicht erhöht, mit einem Maximum für Partikel mit einem Durchmesser von 0,6 µm mit 4,5 #/cm^3. Diese Werte stimmen mit Messungen von Mineralstaub aus verschiedenen Feldexperimenten überein, die in der Vergangenheit durchgeführt und von Adebiyi et al. (2023) zusammengefasst wurden. Zusätzlich wurde der Einfluss der gemessenen Staubschicht auf die Bildung von Mischphasenwolken untersucht, indem die Konzentration an INP unter Verwendung der Parametrisierung von DeMott et al. (2010) berechnet wurde. Für die beobachtete asiatische Staubschicht wurde eine INP-Konzentration von 0,283 (± 0,051) #/L^{-1} ermittelt. Diese Werte stimmen mit gemessenen INP-Konzentrationen während Staubereignissen in Ostasien überein.

Acknowledgement

I would like to thank everyone who helped me in the process of my Master's thesis.

First and foremost, I would like to thank Bernadett Weinzierl for supervising my thesis, giving me constructive feedback and guidance. Thank you for helping me overcome challenges and approach the topic from new perspectives when needed.

Thank you also to Maximilian Dollner, who supported me throughout the process and helped me manage minor and major problems I came across. As well as for taking his time answering any of my questions with patience.

Special thanks to Marina Dütsch for letting me use the online tool of FLEXPART and also adapting it to my requirements. Thank you to Gregory Schill for plots of the volume size distribution with palms data mapped on it. Furthermore, thank you to Ioanna Evangelou for completing FLEXDUST simulations for me and providing me with plots. Thank you to Jingchuan Chen for providing analyzed data of INP concentration for the comparison with my results.

I would also like to thank my colleagues from the aerosol group from whom I got very constructive feedback and support. Especially to my office friends Sophie and Lisa. Thank you, Florian for supplying us with chocolate when needed.

Last but not least, I would like to thank my sister and parents, who supported me during my studies, not only financially but also emotionally.

Table of Contents

1 Introduction and Motivation

An aerosol is defined as a two-component system consisting of a solid or liquid particle, also called aerosol particle, and a carrier gas. In the atmosphere, aerosol particles are suspended in air and are always present, although they vary significantly in their concentrations and characteristics (Hinds, 1999). The concentrations of aerosol particles reach values of up to 10^7particles per cubic centimeter (Seinfeld & Pandis, 2016). The diameter can span over multiple magnitudes between a few nanometers up to 100 µm (Seinfeld & Pandis, 2016), which are categorized into four size modes: *Nucleation mode* (< 10 nm), *Aitken mode* (10 – 100 nm), *Accumulation mode* (100 nm – 1µm) and *Coarse mode* (> 1 µm) (Hinds, 1999). Based on their characteristics, there are different ways to classify aerosol particles, as described by Boucher (2015):

1. A *primary aerosol* is emitted directly into the atmosphere. These particles can be produced by wind friction on a surface or incomplete combustion. *Secondary aerosols* are formed, when gas-phase species condense. In general, these aerosol particle types can be differentiated due to their chemical composition.
2. Another classification distinguishes different origins of the particles. *Anthropogenic sources* include emissions from combustion or human caused wildfires. *Natural sources* are for example volcanos, the ocean or deserts.

From natural sources, mineral dust contributes 48 % of the annual aerosol emissions by mass, resulting in 1500 Tg/yr (Hinds, 1999). The size range of mineral dust particles is usually within the previously defined Accumulation and Coarse mode (Boucher, 2015). Since these sizes span over three orders of magnitude a more detailed classification for mineral dust particles was proposed by Adebiyi et al. (2023) defining the following categories: *Fine* (< 2.5 µm), *Coarse* (2.5 – 10 µm), *Super-Coarse* (10 – 62.5 µm) and *Giant* (> 62.5 µm). Mineral dust particles usually have an irregular shape (Hinds, 1999) and can be distinguished from other atmospheric aerosol particles through their chemical composition. The density of mineral dust particles is assumed to be about 1500 kg/m³ for particles smaller than 1 µm and 2500 kg/m³ for particles with larger diameters (Kandler et al., 2011).

Aerosol particles have a significant impact on the earth's radiative budget and therefore the climate. The radiative effect is measured in W/m² and describes, how aerosol particles infuence the outgoing infrared rediation and the incoming solar radiation. The sign does show, whether the effect is cooling or warming. One distinguishes between the aerosol-radiation interactions and the aerosol-cloud interactions. The first one describes particles interacting directly with radiation by scattering, leading to a cooling effect, and absorption, which has a warming effect. The aerosol-cloud interaction is defined as how the influence of particles on clouds results in a warming or cooling effect (Intergovernmental Panel On Climate Change, 2014). If the water content in a cloud stays the same, while the concentration of CCN increases the cloud droplets decrease in size and increase in number. This leads to an increase in total

surface of cloud particles and resulting from this the albedo of the cloud rises. Additionally, the cloud lifetime is altered, since the formation of precipitation will take longer (Lohmann et al., 2016).

Mineral dust particles directly absorb and scatter shortwave and longwave radiation influencing the atmospheric radiation budget directly. In addition, they function as seeds for cloud droplets and have optimal characteristics for acting as ice nuclei, affecting the appearance and properties of clouds and furthermore alter the hydrological cycle (Choobari et al., 2014). Besides the described effects, mineral dust interacts with the cryosphere, e.g., by reducing reflection when deposited on snow surfaces, and interacts with the biochemistry, by acting as a fertilizer (Kok et al., 2023). The described mechanisms are the most important effects of mineral dust on the climate, both warming and cooling the climate. The estimated result of the net radiative effect of mineral dust is −0.2 (-0.7 to + 0.3) W/m^2. The result shows, that not only the magnitude, but also the sign of the net radiative effect of mineral dust is uncertain (Kok et al., 2023). The changes in the amount of emitted mineral dust due to desertification and changes in human land use can produce a substantial radiative forcing but are still afflicted with a high level of uncertainty (Stanelle et al., 2014).

For mineral dust to be emitted into the atmosphere, the soil moisture must be low and the wind flow must remain undisturbed by vegetation. These conditions are met in desert regions (Boucher, 2015). Mechanical disintegration forms mineral dust particles, which get detached by wind friction and lifted into the atmosphere (Hinds, 1999). After they are lifted, depending on environmental and meteorological conditions, they can be transported over thousands of kilometers (Boucher, 2015; Weinzierl et al., 2017). The size of the particles affects their residence time in the atmosphere. In general, larger particles sediment more rapidly due to

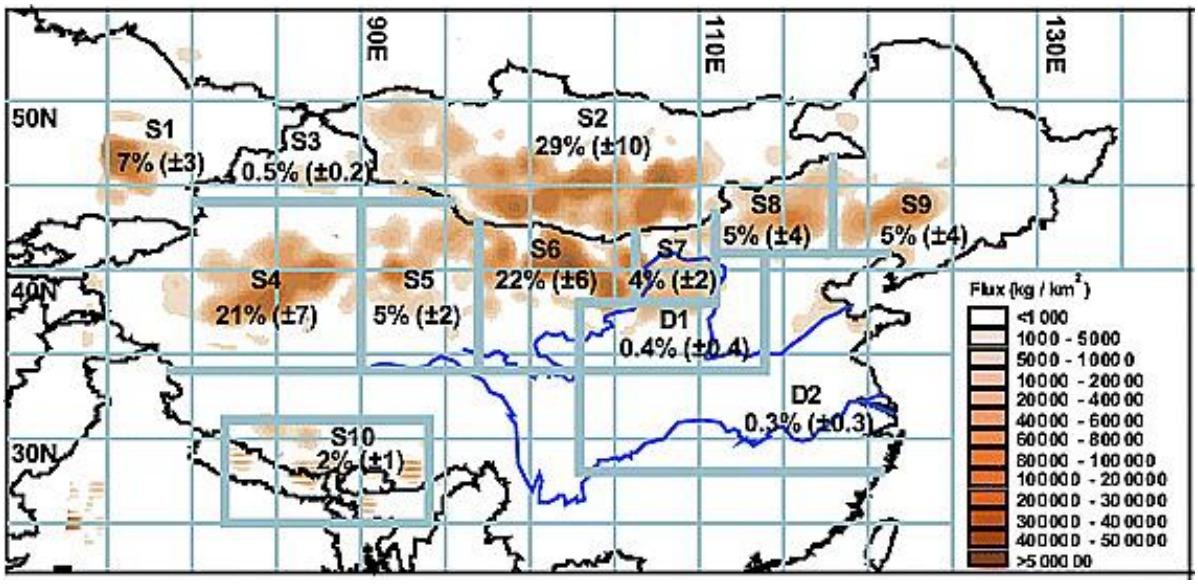

Figure 1: Source Regions of mineral dust in Asia: S1 (Kazakhstan), S2 (Mongolia), S3 (Gurbantunggut Desert), S4 (Taklimakan Desert), S5 (desert in Tsaidam Basin and Kumutage Desert), S6 (Badain Jaran Desert, Tengger Desert and Ulan Buh Desert), S7 (Mu Us Desert and Hobq Desert), S8 (Onqin Daga sandy land), S9 (Horqin sandy land) and S10 (Tibetan Plateau) (Zhang et al., 2003).

gravitational force while smaller particles can stay uplifted for longer periods of time. In addition, the location within the atmosphere is another influencing factor of the residence time. Particles in the upper troposphere and lower stratosphere (UTLS)[1] have a lifetime of up to two years, while those in the lower troposphere typically stay uplifted for a few days to weeks (Bolin et al., 1974).

With 60% of the total global mineral dust emissions north Africa is the main source for mineral dust particles in the atmosphere followed by Asia and the Middle East each contributing about 13 %. It requires a strong vertical updraft for mineral dust particles to enter theUTLS, hence contribution of different sources changes, with North Africa and Asia each contributing around 40 % of the total mass (Froyd et al., 2022). In Figure 1, the ten major Asian mineral dust sources are pictured. Over 70% of the Asian mineral dust particles emitted to the atmosphere are from Mongolia (S2), areas in northern China (S6) and Taklimakan Desert (S4). Badain Jaran, Tengger and Ulan Buh are deserts located in northern China (Zhang et al., 2003).

Depending on source region, the chemical composition of the mineral dust particles can differ from each other quite distinctly. In Figure 2, the mineralogical composition of mineral dust particles of different sources is pictured. Besides Chile, the Asian sources Gobi (including deserts in Mongolia and northern China) and Taklimakan are the only sources with chlorite. Additional contributions to the composition of Asian mineral dust are illite, quartz, feldspars and calcite (Adebiyi et al., 2023).

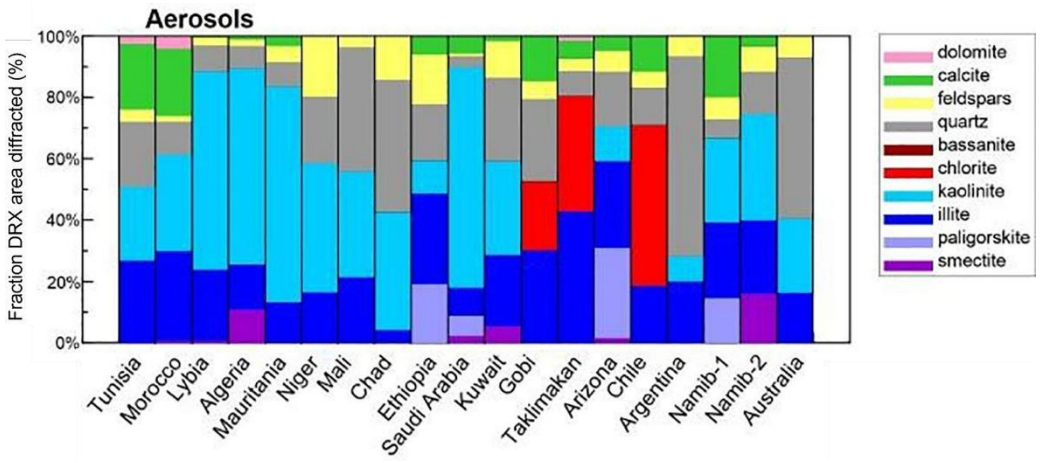

Figure 2: The composition of mineral dust for different sources. The displayed DRX (dynamic recrystallization) fractions are for particles with a diameter smaller than 10 µm (Adebiyi et al., 2023).

One large convective system, strong enough to transport mineral dust particles into the UTLS, is the Asian Summer Monsoon (ASM) (Gottschaldt et al., 2017). The ASM is a dominant global circulation occurring every year between June and August. The ASM includes a largescale anticyclonic circulation, the so-called Asian Summer Monsoon Anticyclone (ASMA), developing

[1] The UTLS is defined as a layer of about 10 km located at +/- 5 km of altitude from the tropopause (Gettelman et al., 2011).

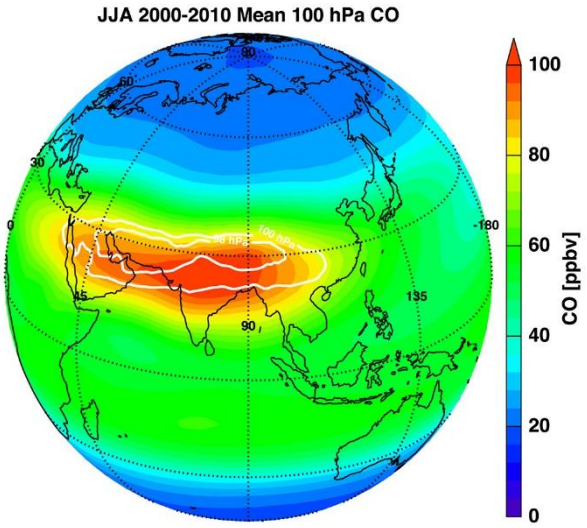

Figure 3: Mean over 10 years for June - August of CO mixing ratio (ppbv) at 100 hPa (Pan et al., 2016).

from the strong heating in the lower troposphere, which leads to a persistent deep convection reaching into the UTLS (Gill, 1980; Hoskins & Rodwell, 1995). This deep convection provides a pathway for trace gases and pollutants into the lower stratosphere (Highwood & Hoskins, 1998). The vertical transport to the UTLS primarily occurs in the eastern part of the anticyclone located at the northeast of India and Nepal, south of the Tibetan Plateau und north of the Bay of Bengal (Pan et al., 2016). Although, the sources of air, transported to the ASMA cover a large portion of southern Asia, the majority pass through a fairly narrow region, where the uplifting pathway is located (Bergman et al., 2013). Once the air masses reaches the UTLS region they remain in the anticyclone, which is the reason for the ASMA showing increased values of tracer gases typical for the troposphere, as e.g., carbon monoxide, pollution and water vapor (Bergman et al., 2013; Randel & Park, 2006). In general, the tropopause of the ASMA region is bulging and therefore creates a bubble of tropospheric air surrounded by stratospheric air (Pan et al., 2016). Eddy shedding of the ASM enables the entry of the lifted tropospheric air into the global UTLS (Honomichl & Pan, 2020). Figure 3 depicts the pollution tracer carbon monoxide (CO) at 100 hPa. This displays the average position of the ASMA region during a ten-year period using the Whole-Atmosphere Community Climate Model, version 4 (WACCM4). The specific daily location of the ASMA depends strongly on the variability of the ASM (Pan et al., 2016). In general, the region influenced by the ASMA is bounded in the north by the subtropical westerly jet stream and in the south by the equatorial easterly jet stream. Resulting in a maximum extend from 10 to 45 °N and 20 to 140 °E (Bossolasco et al., 2021). This extend covers the location of the major Asian mineral dust sources (Zhang et al., 2003), providing the required pathway for mineral dust particles to reach the UTLS (Ma et al., 2019). Especially mineral dust particles originating from the Tibetan Plateau (S10 in Figure 1) and the Taklamakan desert (S4) have a high probability to be lifted form the surface (Xu et al., 2015) and reaching altitudes of the UTLS (Ma et al., 2019). This is due to the geographical proximity to the conduit from the boundary layer to the anticyclone (Bergman et al., 2013).

Even though the general concept of Asian mineral dust entering the UTLS through the ASM is understood, details about the amount and properties of mineral dust in the UTLS as well as its implications on clouds and the atmospheric radiation budget are still linked with a lot of open questions and high uncertainties. Especially more in-situ measurements are needed to gain better understanding about mineral dust in the UTLS, the transport within the Asian Summer Monsoon and the characteristics of these aerosol particles (Ma et al., 2019).

This work investigates observations of mineral dust during the ACCLIP (Asian summer monsoon Chemical and CLimate Impact Project) campaign. From July 31 to September 1 in 2022, the NCAR GV and NASA WB-57 were stationed at the Osan Air Base in the Republic of Korea, conducting up to 17 research flights each. The overall aim of ACCLIP was to investigate the pathways of aerosol particles to the global UTLS through the ASM and to analyze the chemical content of these air masses (Pan et al., 2024). The campaign and its objectives will be introduced in more detail in chapter 3.1.

The following research questions will be addressed:

1. Are there periods of mineral dust particles measurements during ACCLIP?
2. What are the characteristics of the number size distributions of the investigated mineral dust layers?
3. What are the geographical source regions of these mineral dust particles?

In order to answer these research questions, data from different instruments, which were installed on the high-altitude research aircraft WB-57, will be analyzed. The main instrument for this study is the UNIVIE-CAPS, which measures particles between 0.5 to 930 µm. This instrument can contribute in analyzing mineral dust particles in the UTLS and will be introduced in section 3.2.1. Besides answering the scientific research questions, the data processing of the UNIVIE-CAPS is a major part of this thesis, described in section 3.3.

2 Theoretical Background

In this chapter the necessary theoretical background is provided for the understanding of this thesis. First, microphysical properties of particles are further explained, starting with the equivalent diameter, particle concentration and size distribution, chemical composition and aerosol mixing. It also explains different transport mechanisms in the atmospheric circulation, including vertical and horizontal transport, monsoons, and removal processes, latter divided in the description of wet and dry deposition.

2.1 Aerosol Basics

The majority of atmospheric aerosol particles are not spherical, additionally other characteristics like density or charge of the particles are usually unknown. In order to be able to compare particles nevertheless, *equivalent diameters* are used. Depending on what characteristic is important for the measurement, different equivalent diameters can be defined (Seinfeld & Pandis, 2016). For example, the mass equivalent diameter is the diameter of a sphere with the same mass as the aerosol particle being described. Another way to assign a size to a particle is to take the area of particle's cross-section and define a circle with the same area. The diameter of this circle is called the projected area-equivalent diameter. The amount of scattered light is used to introduce the optical equivalent diameter (Kulkarni et al., 2011). In this case the relation between detected signal and diameter has been defined for an instrument by spherical calibration particles (Hinds, 1999). In general, any characteristic of the aerosol particle can be used to define an equivalent diameter (Kulkarni et al., 2011), however different definitions do not match completely. Therefore, it is important to note which aspect of the aerosol particle is represented with the given diameter (Hinds, 1999).

The concentration of particles is the description of aerosol particles per unit volume, which in most cases is either m^3 or cm^3. Different types of particle concentration can describe any specific property, the most common ones are number, mass and volume concentrations (Kulkarni et al., 2011). In contrast, gas measurements are usually given as volume or mass ratio in parts per million (ppmv or ppmm). These units are not used for aerosol particles, since the concentrations are very low when expressed in this way (Hinds, 1999).

Both, temperature and pressure are variable, therefore to compare the particle concentration of an air mass, they are often calculated to standard temperature and pressure (STP) conditions. These standard conditions are defined as a pressure of 1013.25 hPa and temperature of 273.15 K (Kulkarni et al., 2011). For an aerosol population the particles can be monodisperse, in this case all particles have the same size within a spread of less than 10 - 20 %, or polydisperse, in which the size range of particles is wider (Kulkarni et al., 2011).

Since for polydisperse aerosol particles the diameters can span over multiple magnitudes, the description by a particle size distribution is important. The simplest representation is a histogram. For this, the particles are sorted in bins, with an upper and a lower limit of the

diameter (Kulkarni et al., 2011). The lower limit diameter of a bin is the same, as the upper limit diameter of the previous interval (Hinds, 1999). The number size distribution describes how many particles are counted in each size bin. To correct for different bin widths, the histogram is normalized by dividing the concentration with the bin width (Seinfeld & Pandis, 2016), resulting the number of particles per unit of size interval (Kulkarni et al., 2011). The sum of all bins is the total number of particles N

$$N = \sum_i (h_i' \Delta D_i) = \sum_i n_i \quad , \tag{1}$$

where h_i' is the counts in the i-th bin in number per length, and ΔD_i the width (Hinds, 1999).

For a functional representation of the aerosol size distribution $n_N(D_p)$, the bin width is decreased to infinitesimally small intervals dD_p (Hinds, 1999), where $n_N(D_p)$ describes the number of particles with a diameter in the range D_p to $(D_p + dD_p)$ per cm^3. As a result, the total number of particles can be expressed as the continuous function of the particle's diameter (Seinfeld & Pandis, 2016):

$$N = \int_0^\infty n_N(D_p) dD_p \tag{2}$$

Since the particles diameter span over multiple magnitudes commonly a logarithmic scale is used to show the concentration of particles (Hinds, 1999). Furthermore, aerosol size distributions are typically lognormal, so they look like a bell-shaped curve, when plotted on a logarithmic scale, exemplarily illustrated in Figure 4 (Kulkarni et al., 2011).

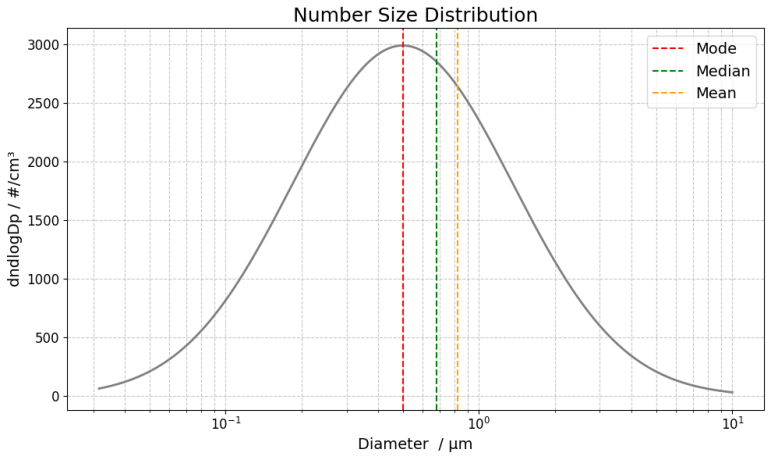

Figure 4: Number size distribution, with the concentration of particles on the y axis and the diameter in lognormal on the x axis.

Statistical parameters for particle size distributions are used to describe aerosol populations and provide a useful measure to compare different aerosol populations. The most common ones are the mode, median and mean diameter (Boucher, 2015), visible in Figure 4. The mode describes a maximum in the distribution. There can be more maxima, resulting in a multimodal distribution (Kulkarni et al., 2011). The median diameter is defined as half of the particles being larger and the other half being smaller sizes, while the mean diameter is an arithmetic average of all particle sizes (Boucher, 2015). In addition, the spread of the size distribution can be described by the standard deviation (Kulkarni et al., 2011).

Besides the number of particles, the mass or surface are commonly represented in particle size distributions (Boucher, 2015).

The chemical composition of aerosol particles has an important influence on their behavior in the atmosphere. It determines the hygroscopicity of the particles, their optical properties, as well as their role as cloud condensation or ice nuclei (Boucher, 2015). Mineral dust particles are the dominating ice nuclei particles in the atmosphere (Cziczo et al., 2013) and therefore have a significant impact on cirrus cloud formation processes (Froyd et al., 2022).

Atmospheric aerosol particles are a mixture of different elements. One distinguishes between external and internal mixtures; they are schematically pictured in Figure 5: Illustration of aerosol mixing state, adapted from Riemer et al. (2019) and Boucher (2015). An external mixture describes a mix of different particles, where each particle is chemically pure – illustrated in Figure 6 by the black and white spheres. An aerosol population with a perfect internal mixture consists of particles, with more than one chemical species but the chemical composition of all particles is identical. In a realistic scenario, an airmass of aerosol particles is neither a completely external nor only an internal mixture (Boucher, 2015). As an example, mineral dust particles are primary aerosols, composed of different chemicals. In addition, a coating of secondary species can form on their surface, which can alter the properties, e.g. hygroscopicity, of the particles (Riemer et al., 2019).

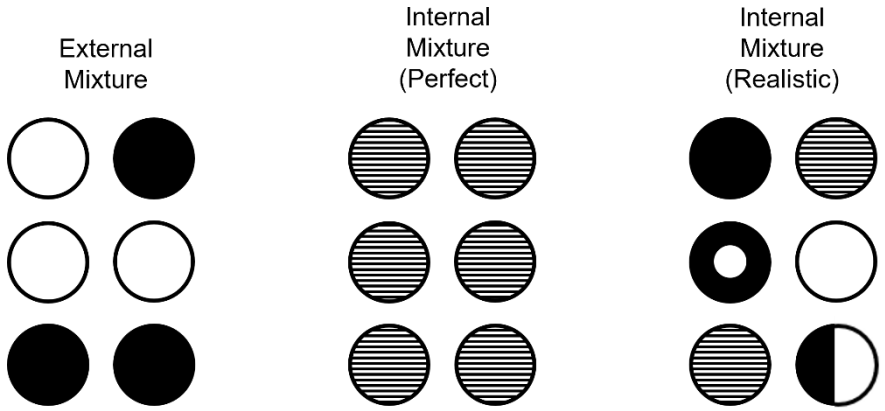

Figure 5: Illustration of aerosol mixing state, adapted from Riemer et al. (2019) and Boucher (2015).

Aerosol particles have an impact the microphysical properties of clouds by acting as cloud condensation nuclei (CCN) or ice nucleating particles (INP) (Boucher, 2015; Froyd et al., 2022). On the surface of CCNs, water vapor can condense, leading to the formation and growth of cloud droplets. This mechanism occurs, when the atmosphere is supersaturated with respect to water (Lohmann et al., 2016). For the formation of ice crystals, one distinguishes between homogeneous and heterogeneous nucleation (Boucher, 2015). The first one describes the freezing process of solution particles, hereby no other aerosols are needed besides the initial CCN (Lohmann et al., 2016). At temperatures above -38 °C heterogeneous freezing dominates the ice crystal formation, for which aerosol particles, acting as INPs, are necessary. Here, one distinguishes between deposition and freezing nucleation. While freezing nucleation involves a liquid state, deposition nucleation describes supersaturated vapor directly depositing on an

INP (Vali et al., 2015). Clouds at temperatures above 0 °C are exclusively composed of liquid droplets, while when the temperature drops below -38 °C they are solely ice (Lohmann et al., 2016). In between these temperature regimes, mixed-phase clouds occur. Here, the cloud particles can be liquid, solid or both (Boucher, 2015).

Whether an aerosol particle acts as CCN or INP, depends on its size and chemical composition. Mineral dust particles show ideal INP characteristics, which leads to an ice crystal formation at lower relative humidity over ice of 107 to 117 % and higher temperatures between -10 and -16 °C in comparison to other INPs (Lohmann et al., 2016; Zimmermann et al., 2008).This makes the abundance of mineral dust a key factor of cloud formation at temperatures below 0 °C (Froyd et al., 2022).

2.2 Transport Processes in the Atmosphere

Mineral dust particles can be transported over thousands of kilometers before they are deposited in regions far away from their source. This plays a key role in the ecosystem, since mineral dust acts as fertilizer for the ocean productivity and e.g., the Amazon rainforest (Schepanski, 2018). Additionally, mineral dust particles are an important factor for cloud formation processes, thus after a long-range transport, the particles can influence clouds in regions in far distance of their source. Therefore, the transport within the atmosphere, as well as removal processes are important to understand which will be explained in this chapter.

2.2.1 Atmospheric Circulation

Vertical Transport

The vertical motion of atmospheric air parcels[2] is described by the stability of the atmosphere, where the difference between the temperatures of the air parcel and its surrounding determines whether the conditions are stable, neutral or instable. For stable conditions a displacement of an air parcel leads to a push back to its starting altitude, i.e., if an air parcel is moved upward, its temperature will be colder than the new surrounding leading to a negative buoyant force which pushes the air parcel back to the starting point. If the air parcel remains at the new altitude, because the temperature of the air parcel and the new surrounding is equal, the atmosphere is defined to be neutral. For instable conditions, the buoyant forces act in the direction of the initial displacement, i.e., if a parcel was lifted it will continue to rise due to the positive buoyant forces as the parcel will have a higher temperature than the new surroundings. These processes determine, if aerosol particles are transported into the atmosphere (Seinfeld & Pandis, 2016).

During the day the ground absorbs solar radiation, causing the temperature of the lowest layer of air to rise. The temperature difference creates an atmospheric instability and air parcels begin to rise. This process is called atmospheric convection (Holton, 2004). As an air parcel is

[2] An air parcel refers to a conceptual volume that is approximately the size of tens of centimeters in each dimension. It holds the essential characteristics of air and is thermally insulated from its surroundings (Lohmann et al., 2016).

lifted, it experiences a decrease in ambient pressure, which causes it to expand and subsequently results in a decrease in temperature. As the temperature decreases, the relative humidity increases. Thus, as an air parcel is displaced upwards, water vapor can begin to condense on aerosol particles, leading to the formation of clouds (Seinfeld & Pandis, 2016).

Horizontal Transport

The combination of pressure gradients due to uneven heating of the surface and the Coriolis force, resulting from the Earth's rotation, generates the global wind systems of the Earth. The three-cell model is very simplified but gives a good overview of the large-scale pattern of atmospheric circulations. The three cells are called Hadley cell, Ferrel cell, and Polar cell and are schematically shown in Figure 6 (Seinfeld & Pandis, 2016).

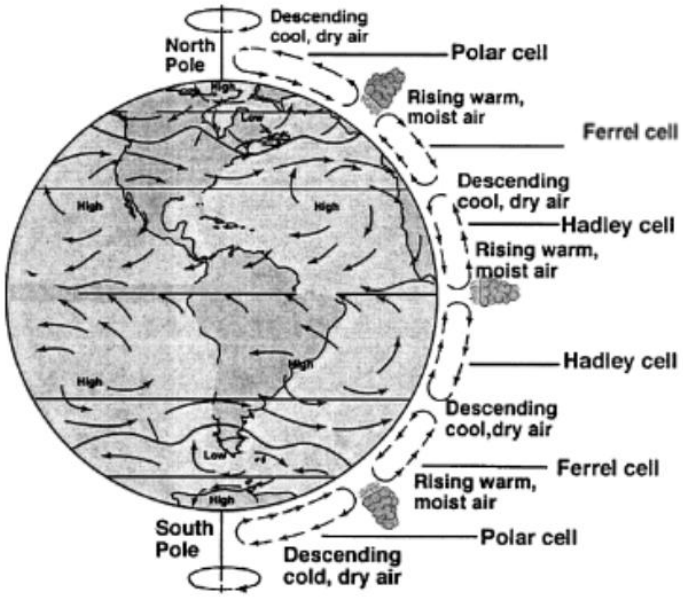

Figure 6: Representation of the atmospheric global circulation adapted from Seinfeld and Pandis (2016).

The Hadley cells expand form the equator to 30° to 35° north and south of the equator and are dominated by steady trade winds. The converge at the equatorial zone and result in the so-called intertropical convergence zone (ITCZ), an area with low pressure. Moist air is warmed at the equator by solar radiation and rises, resulting in air near the ground flowing back, replacing these air masses. This leads to an easterly wind due to the Coriolis force (Roedel & Wagner, 2017). At 30° to 35° the air is descending and can then move towards the equator, closing the circulation of the Hadley cell. At this latitude the subtropical Jetstream is formed with windspeeds usually exceeding 30 m/s occurring in the upper troposphere (Seinfeld & Pandis, 2016). Air that is moving in direction of the pole will then lead to westerly winds. The westerly winds reach latitudes of about 70° and are impacted by fronts, low- and high-pressure systems, which makes them less stable than trade winds. The resulting circulation between latitudes of 30 ° to 70 ° is called Ferrel cell (Roedel & Wagner, 2017). At 70 ° latitude north and south of the equator, the polar easterly Jetstream is located. From there, air is moving further

north and south and descends above the poles. This leads to high pressure and the air then flows back towards the equator. This is defined as the Polar cell (Seinfeld & Pandis, 2016).

Monsoon

Any periodically reversing circulation system generally is referred to as a monsoon and is created due to different thermal properties of surfaces like sea and land. The surface temperature over land usually rises faster than over the ocean resulting in high pressure over sea and low pressure over land. Monsoons influence most of the tropics but the Asian summer monsoon is the largest monsoon circulation, which has been introduced in chapter 1 (pp. 3-4). The Indian subcontinent's climate is entirely controlled by this monsoon, which results in warm, rainy summers and chilly, dry winters. The temperature gradient leads to cumulus convection and consequential to a release of latent heat. This rises the tropospheric temperature (Holton, 2004). The ASM has a complex structure with two subsystem (Indian summer monsoon and East Asian summer monsoon) which interact with each other (Yihui & Chan, 2005). They both drive and influence the ASMA, where the two main pathways for aerosol particles to reach this circulation in the UTLS are located at the Himalayan foothills and over central and southwestern China. The ASMA is not completely isolated for its surroundings and therefore exchanges happen as a result of which aerosols and tracer gases are transported to the global UTLS (Randel & Park, 2006). According to Yu et al. (2017) the ASM contributes around 15 % of the norther hemispheric stratospheric aerosols per year.

2.2.2 Removal Processes

Wet Deposition

Wet deposition is the main sink for aerosol particles in the atmosphere (Seinfeld & Pandis, 2016) and includes in-cloud and below-cloud scavenging. During in-cloud scavenging, an aerosol particle either acts as CCN or a cloud droplet collides with aerosol particles. When the cloud droplets reach sizes where they start to precipitate, incorporated aerosol particles will fall down with rain droplets (Boucher, 2015). Cloud droplets typically have a radius of around 0.005 mm, when reaching a radius of 0.1 mm drizzle drops are formed. The radius of raindrops usually varies between 0.25 to 5 mm (Lohmann et al., 2016). Below-cloud scavenging describes the process when raindrops collide with aerosol particles while they are falling down (Boucher, 2015).

Dry Deposition

Dry deposition is defined as the transport of particles from the atmosphere onto the surface without precipitation (Seinfeld & Pandis, 2016). This includes the sedimentation (gravitational settling) of aerosol particles and the deposition due to turbulent flux (Boucher, 2015).

An aerosol particle in still air is exposed to the following forces: drag, gravity, and buoyancy. The buoyancy can usually be neglected, since omitting the buoyancy causes effectively an error of roughly 0.1 %. The drag force (air resistance) acts opposite to the force of gravity and the equilibrium of both forces results in a terminal settling velocity. When this velocity is reached,

the particle does not accelerate any more. It is proportional to the square of the diameter of the aerosol particle and therefore increases rapidly with size (Hinds, 1999). In the troposphere the process of sedimentation is dominating the dry deposition for aerosol particles in the coarse mode (Boucher, 2015).

In comparison to the troposphere, the stratosphere, located at between 8 – 55 km of altitude, shows slow vertical motion (Seinfeld & Pandis, 2016) and the aerosol residence time can be in the magnitude of years. Due to the stable stratification and low water vapor content clouds in the stratosphere are rare. Therefore, gravitational settling is the dominant process of deposition of aerosols in these altitudes (Boucher, 2015).

3 Methods

An overview of the ACCLIP campaign is provided at the beginning of this chapter. It contains the goals of the campaign and a summary of the various flights that have been performed. After that, important instruments used in this study are shortly described. The UNIVIE-CAPS raw-to-final data processing is explained in section 3.3. This includes introducing the time offset and the cloud indicator. In section 3.4 the determination process of mineral dust measurement periods is explained, in addition to the FLEXPART backward trajectory calculations.

3.1 ACCLIP campaign overview

The Asian summer monsoon Chemical and CLimate Impact Project (ACCLIP) is a National Aeronautics and Space Administration (NASA) and the National Science Foundation's National Center for Atmospheric Research (NCAR) funded aircraft campaign, with the primary goal to gain a better understanding about the impact of Asian gas and aerosol emissions on global scale, and the transport of these emissions through the ASM (Pan et al., 2024). The following research objectives for the dynamical, chemical and microphysical measurements in the region of the ASMA were defined beforehand (UCAR, 2024):

> *the transport pathways (vertical range, intensity, and time-scale) of the ASM uplifted air from inside of the anticyclone to the UTLS*
>
> *the chemical content of air processed in the ASM for UTLS ozone chemistry, and short-lived climate forcers*
>
> *the information on aerosol size, mass and chemical composition for determining the radiative impact*
>
> *the water vapor distribution associated with the monsoon dynamical structure*

In order to answer these research questions, two research aircrafts were stationed at the Osan Air Base in the Republic of Korea, conducting flights over the western pacific from July to September 2022. The NCAR G-V and the high-altitude NASA WB-57, conducted 15 and 17 research flights accordingly (Pan et al., 2024). Since the analysis of this study is focused on the observations made with the WB-57, only WB-57 related information are presented in the following. Table 1 lists all flights of the WB-57, including their date, flight name, time offset (which will be explained in chapter 3.3.3) and the objective of the flight.

*Table 1: Overview of all flights, including time offset and objective. The time off sets marked with * are the mean of all determined time offsets. The objectives were only defined for the research flights in Asia.*

Date	Flight name	Time offset in s	Objective
14 Jul 2022	WB-Test	-6.6	
16 Jul 2022	WB-RF01	-6.6	
18 Jul 2022	WB-RF02	-6.6 *	
21 Jul 2022	WB-OT1	-6.6 *	
21 Jul 2022	WB-OT2	-6.4	
24 Jul 2022	WB-OT3	-6.5	
25 Jul 2022	WB-OT4	-6.5	
27 Jul 2022	WB-OT5	-6.6 *	
2 Aug 2022	WB-RF03	-6.6 *	sample a streamer
4 Aug 2022	WB-RF04	-6.7	"REThinC" cirrus sampling
6 Aug 2022	WB-RF05	-6.5	sample shed air, to make more cirrus measurements
12 Aug 2022	WB-RF06	-7.0	sample a shed air mass, and possibly sample cirrus
13 Aug 2022	WB-RF07	-6.6	sample streamers of shed air masses
15 Aug 2022	WB-RF08	-6.5	sample shed air overhead and possibly to sample cirrus
16 Aug 2022	WB-RF09	-6.7	sample the Asian anticyclone lobe, to sample cirrus
19 Aug 2022	WB-RF10	-6.5	sample anticyclone overhead, possibly to sample cirrus, coordination w./ NCAR GV.
21 Aug 2022	WB-RF11	-6.7	sample air being shed form the anticyclone
23 Aug 2022	WB-RF12	-6.8	sample air being shed from the anticyclone.
25 Aug 2022	WB-RF13	-6.6	sample air mass shed from the anticyclone, to do coordinated flight w/ the NCAR GV
26 Aug 2022	WB-RF14	-6.7	sample air being shed from the anticyclone, to sample high clouds
29 Aug 2022	WB-RF15	-6.7	sample the edge region of the anticyclone
31 Aug 2022	WB-RF16	-6.7	sample outflow from a typhoon, to sample nearby shed anticyclone air
1 Sep 2022	WB-RF17	-6.7	sample air being shed from the anticyclone
9 Sep 2022	WB-RT01	-6.6	
12 Sep 2022	WB-RT02	-6.7	
13 Sep 2022	WB-RT03	-6.7	
14 Sep 2022	WB-RT04	-6.4	

In Figure 7 the flight tracks of the WB-57 are plotted on a world map. In North America the test flight (WB-TEST) and the first two research flights (WB-RF01 and WB-RF02) are located.

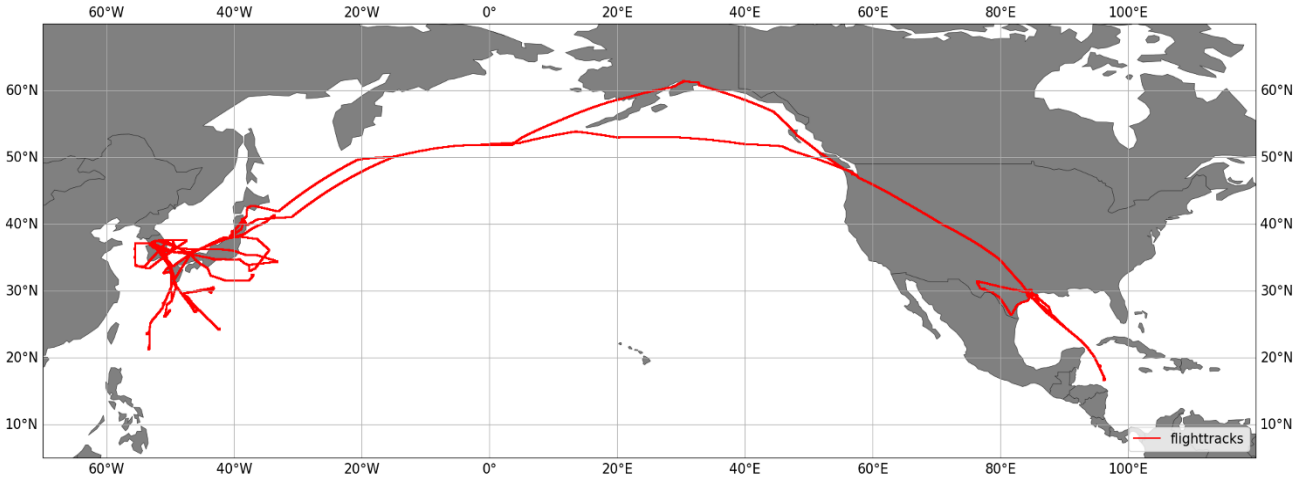

Figure 7: Map of all flight paths of the WB-57 during the ACCLIP campaign.

Over the pacific the transit flights (WB-OT and WB-RT) took place and starting from Korea the research flights (WB-RF02 to WB-RF17) are shown.

3.2 Instrumentation

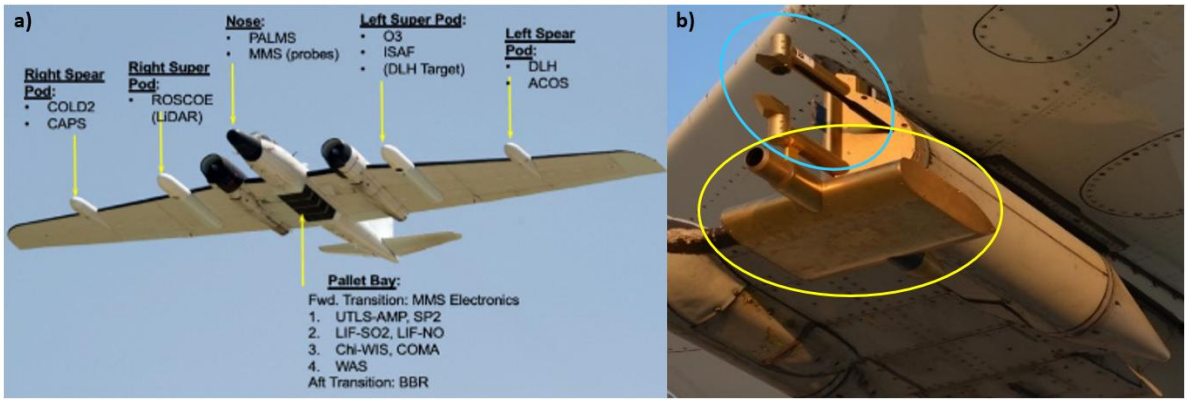

Figure 8: a) Payload of the WB-57 during the ACCLIP campaign (UCAR, 2024) b) UNIVIE-CAPS, mounted on the wing of a different research aircraft, circled in blue is the CIP and in yellow the CAS (Dollner et al. 2024).

In Figure 8 a) the mounting position of the instruments on the WB-57 are illustrated (UCAR, 2024). The instrumentation covers measurements of meteorological parameter, trace gases, and optical, microphysical and chemical properties of aerosol particles as well as properties of clouds. Additionally, an instrumentation for upward and downward remote sensing was installed. In the data archive of the ACCLIP campaign (Aknan, 2024) the available products of each instrument are provided.

In the following, instruments of the WB-57 payload, which are used in this thesis, are described.

3.2.1 CAPS – Cloud, Aerosol, and Precipitation Spectrometer

The main instrument of this study is the University of Vienna's Cloud, Aerosol, and Precipitation Spectrometer (UNIVIE-CAPS, Droplet Measurement Technologies Inc, Longmont, USA). The instrument measures aerosol and cloud particle size distributions in the size range between nominally 0.5 and 930 µm. For ACCLIP the UNIVIE-CAPS was mounted at the wing of the WB-57, as visible in Figure 8. CAPS consist of two main parts, the Cloud and Aerosol Spectrometer (CAS) and the Cloud Imaging Probe (CIP). Besides the CAS and CIP, there are some additional sensors included in the CAPS measuring the true airspeed, pressure, relative humidity, temperature, and liquid water content. The following explains the working principals of the CAS and CIP components based on Baumgardner et al.(2001), Dollner (2022) and Dollner et al. (2024).

1. CAS – Cloud and Aerosol Spectrometer

The CAS, circled in yellow in Figure 8 b), is an optical spectrometer. It measures particles with a diameter between nominally 500 nm and 50 µm. The measurement principal is that particles passing the measurement volume scatter light of a laser with a wavelength of 658 nm. The forward scattered light is collected by a detector covering the angles between 4.2° to 13.2°. The signal amplitude of the measured scattering provides information about the size of the particle. The optical equivalent particle diameter is obtained by the application of the instruments calibration results, where the relation between signal and particle size is defined. With this approach, the influence of the composition and non-sphericity of the particles is neglected since the optical equivalent diameter is reported.[3] In addition, a masked detector determines, whether the particle is within the depth of field of the instrument. The backscattered light between 168° and 176° is detected by two backward detectors. One provides information about the particle's shape and the other one gives additional information about the size of the particle and the fraction of polarization of the backscattered light. For this study, only the measurements of the forward detector were used.

The data output is in the format of a standard time-series with a defined resolution (usually 1 or 10 Hz) and in single particle data (Particle-by-Particle, pbp). More information about the data processing will be given in section 3.3.

[3] Additionally, the CAS does provide the possibility to consider composition and non-sphericity of measured aerosol particles. Though this is not used in this work.

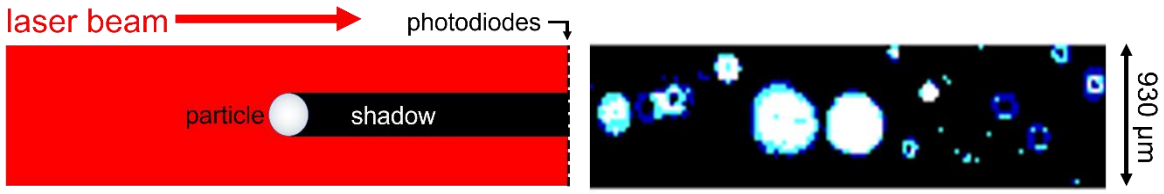

Figure 9: Function of an optical array probe, adapted from Dollner (2022). On the left it is schematically shown, how a particle passes through the laser beam and creates a shadow on the array of photodiodes. On the right, the resulting images of the CIP are pictured with the maximum width of 930 µm.

The CIP is covering a size range of 15 to 930 µm and is circled in blue in Figure 8 b). The measurement technique is schematically shown in Figure 9. When a particle passes the 658 nm laser beam, it produces a shadow on a linear array of photodiodes (shown as dashed line). A single recording of the state of the diode array is called slice and the recording frequency is proportional to the true airspeed of the plane. Combining the recorded slices result in a complete image, from which the size and shape of particles can be obtained. The UNIVIE-CIP is a greyscale version of the instrument that records the images of the particles with multiple intensity levels, which for the UNIVIE-CIP are 30, 50, and 70%. An example of the resulting images is pictured in Figure 9 on the right. There, also the intensity of the shadow is visible in the form of different blue tones. The data output is in the format of a standard time-series with a defined resolution (usually 1 or 10 Hz) and an image of every recorded particle. More information about the data processing will be given in section 3.3.

3.2.2 MMS – Meteorological Measurement System

MMS stands for Meteorological Measurement System and applies high-precision sensors and an individual navigation system for exact air motion measurements (Scott et al., 1990). For ACCLIP, MMS was located in the nose of the WB-57 as pictured in Figure 8 a). MMS provides their data in 1 Hz and 20 Hz resolution. In Table 2 the primary products, including the precision and accuracy are listed (Scott et al., 1990).

Table 2: Primary data products of MMS.

Primary Products 1-20 Hz	Precision	Accuracy
Pressure	± 0.003 mb	± 0.3 mb
Temperature	± 0.05 K	± 0.3 K
Horizontal Wind	± 0.1 m/s	± 1.0 m/s
Vertical Wind	± 0.05 m/s	± 0.3 m/s

In total 25 products are available from MMS, besides the primary products the following ones are of significance for this thesis: longitudinal and latitudinal position, and altitude (Aknan, 2024).

3.2.3 PALMS – Particle Analysis by Laser Mass Spectroscopy

The Particle Analysis by Laser Mass Spectroscopy (PALMS) preforms in-flight measurements of the chemical composition of single aerosol particles. The second-generation PALMS was constructed to measure stratospheric aerosols and mounted into the nose of the research aircraft WB-57 (Thomson et al., 2000). The working principle is described by Murphy & Thomson (1995): After an aerosol particle enters the instrument it passes a laser beam. A photo multiplier tube collects the light that the particle scatters and the signal triggers an excimer laser. A second laser pulse vaporizes and ionizes a fraction of the particle and the ions are accelerated down a time-of-flight (TOF) mass spectrometer. The resulting spectra reveals the composition of the particles.

PALMS provides number fractions as a data product of the following classifications of particles: pure organics or pure sulfate, nitrogen-rich, biomass burning, elemental carbon, mineral/metallic, meteoric, alkali salt, sea salt, heavy oil combustion, and unclassified (Aknan, 2024). In addition, particle-by-particle (pbp) data and size distributions with PALMS data mapped on was provided by the PALMS Team (Acknowledgement to Gregory Schill).

3.2.4 DLH – Diode Laser Hygrometer

DLH is short for Diode Laser Hygrometer and measures H_2O vapor by differential absorption. The set-up is custom-built for each aircraft and consist of a laser transceiver and a target made out of high reflecting material. The mounting positions are visible in Figure 8. In the algorithm calculating the H_2O vapor besides the absorption signal, temperature, ambient pressure and spectroscopic parameters are taken into account (Diskin et al., 2002). DLH provides H_2O in ppmv (parts per million in volume) with a precision of 0.05 ppmv and accuracy of 0.5 ppmv. In addition, data of relative humidity in respect to water and ice (RH_w and RH_i) is provided in 1 Hz and 20 Hz resolution with an accuracy of 10 % (Aknan, 2024).

3.2.5 Chi-WIS – Chicago Water Isotope Spectrometer

The Chicago Water Isotope Spectrometer (Chi-WIS) measures water vapor and HDO (^2H_2O) and provides one data point every five seconds (Aknan, 2024). The instrument is an off-axis integrated cavity output absorption spectrometer with a mid-infrared tunable diode laser (Sarkozy et al., 2020).

3.3 Data processing

3.3.1 CAPSLib

Dollner (2022) developed the CAPSLib algorithm in Python to process the raw measurement data of the UNIVIE-CAPS. The size distribution of the CAS is determined for equivalent diameter with refractive indices of 1.31, 1.33, 1.52 and 1.56 respectively. The calculated size distributions are valid for particles in ambient conditions of the measurement. The CAPSLib loads the output files of the CAPS instrument and the required data of MMS and DLH each in

20 Hz resolution. Additionally, the processing requires CAS calibration data and campaign specific information.

The algorithm CAPSLib enables to process the data and gives a first overview on how the instrument performed, as well as the measurement itself. The quality of the measurement is guaranteed by the application of a quality flag, both for the CAS and the CIP. The processed data is available for 1 Hz and 10 Hz resolution. For the CAS 15 size bins are calculated and for the CIP 62 different sizes are distinguished. The final data product provided in the campaign data archive includes particle number concentration for four size bins of the CAS with the following size ranges: Acc=0.47 to 1.0 µm, Coa1=1.0 to 10.0 µm, Coa2=10.0 to 30.0 µm, Coa3=30.0 to 50.0 µm. The number concentrations are calculated for a sulfate optical equivalent diameter and for standard temperature and pressure (STP) conditions. In addition, the cloud indicator (described in chapter 3.3.2) is reported in a separate data product file. Both, the particle number concentrations, as well as the cloud indicator are provided in 1 Hz resolution.

3.3.2 Cloud indicator and cloud flag

Table 3: Cloud indicator and cloud flag classification in data product.

Cloud Indicator		**Cloud Flag**	
Cloud free	0	Cloud free	0
ACTR	1		
Liquid cloud	2	In cloud	1
MPTR	3		
Cirrus clouds	4		

The cloud indicator is an algorithm detecting measurement periods of clouds developed by Dollner et al. (2024). It distinguishes between cloud free periods, aerosol cloud transition regime (ACTR), liquid clouds, mixed phase temperature regime (MPTR), and cirrus clouds. The criteria take temperature, relative humidity, number concentration and the cloud-aerosol volume factor into account. The latter is independent of the cloud type and is defined as the ratio of volume concentrations for size ranges dominated by aerosol to cloud particles. The cloud flag results from the cloud indicator. It is as a data product, provided as visible in Table 3 (Dollner et al., 2024).

Cloud flag for RF 03

For the flight “RF03”, DLH could not provide data and since relative humidity is inevitable for the cloud flag from the cloud indicator algorithm, a different approach was chosen to cloud flag the data:

During ACCLIP most of the measurements took place within the UTLS and in these altitudes large aerosol particles have a short residence time. Therefore, starting from a certain particle size, it is very probable that the measured particle was a cloud particle and not an aerosol particle. Applying this assumption, the CIP measurements can be used to obtain periods, when

the aircraft was flying in clouds. For this, a size threshold for the CIP measurements is defined. If a particle of a certain size or larger is measured, the cloud flag is set to one. Research flight RF 16, where the cloud indicator data is available, was used as a test case to define the threshold size for the cloud flag from the CIP measurements. The results of the calculation are visible in Figure 10.

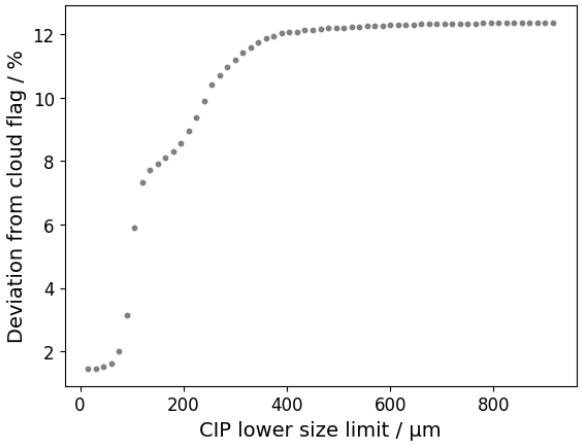

Figure 10: The lower limit of diameter in µm is shown on the x axis, plotted against the deviation from the cloud flag calculated with the algorithm of Dollner et al. (2024).

The deviation of the new approach of the cloud flag from the cloud flag of Dollner et al. (2024) is shown in percentage of the total 17691 measurement values available for RF16. At the CIP's lower size limit of 15 µm, the greatest number of matching results is obtained, indicated by a low deviation. As an outcome, the CIP cloud flag is defined as follows: when the CIP measures a particle, it is defined as “in cloud” - periods with zero particles detected by the CIP instrument are considered cloud-free. This approach was used to calculate the cloud flag for RF03. A calculation of the cloud indicator product, differentiating the cloud types is not possible with the CIP approach.

3.3.3 Time Offset

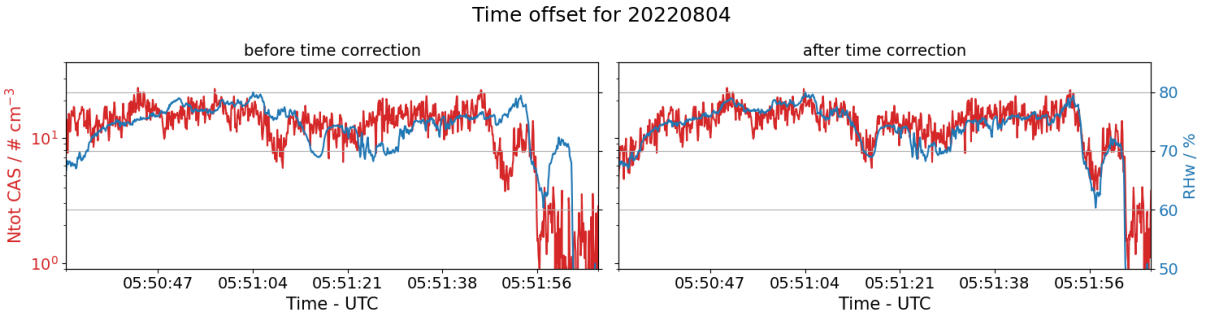

Figure 11: Total number concentration (N_{tot}) of the CAS and relative humidity of DLH before and after the time synchronization.

During an aircraft campaign, several instruments are installed on one aircraft. Due to potentially not synchronized clocks of the data acquisition systems as well as instrument response and/or tubing length, the measurements of different instruments can be shifted in time. In order to synchronize the measurements in time, the time offset for each flight and instrument must to be determined. For the ACCLIP campaign, the DLH instrument was defined

as the primary instrument to which all other instruments should synchronize. For the CAPS, the best approach to calculate the time offset is described as follows. When the aircraft enters a cloud, the relative humidity as well as the measured total number concentration of the CAS rises. Therefore, the DLH relative humidity data (blue) is compared to the total number concentration of the CAS (red) as shown in Figure 11 for RF04 on August 4th 2022. The left plot shows the measurements without time correction applied. By shifting the time of the total number concentration of the CAS the time offset for each flight can be determined. For RF04, the value of the offset is -6.7 seconds. The time offset values for each individual flight are listed in Table 1. Since for some flights no distinct patterns could be identified or DLH data is not available the average of all time offsets was applied. These flights are marked with a star in Table 1.

3.4 Data analysis

3.4.1 Identification of mineral dust measurement periods

In order to identify observations of the WB-57 within mineral dust layers, data from the PALMS instrument was analyzed in detail. The PALMS particle-by-particle data provides the main chemical composition and an aerodynamic diameter of every single detected particle, which can be used to detect periods of mineral dust measurements in the ACCLIP dataset. The following explains the analysis procedure and data combination of the PALMS and CAPS observations.

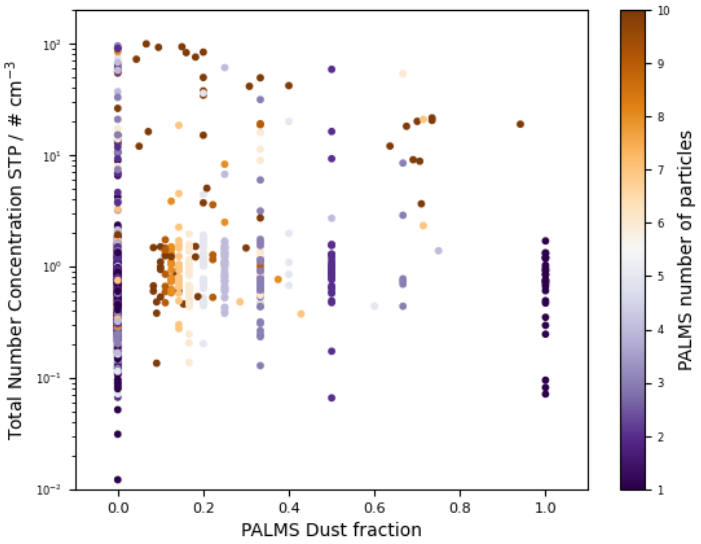

Figure 12: The PALMS mineral dust fraction is plotted against the total number concentration of CAPS. The color code represents the number of total particles measured by PALMS within 90 seconds.

Since this study is focused on coarse mode mineral dust layers, PALMS pbp data was filtered for cloud-free periods using the cloud flag and for particles with a diameter larger than 0.5 µm were considered. One needs to keep in mind, that PALMS measures aerodynamic and the CAS an optical equivalent diameter. Although, for mineral dust particles within the fine mode these are comparable (Huang et al., 2021) which is the case in this study. Therefore 0.5 µm was

chosen for the lower limit diameter of PALMS, since it is the lower limit of the CAS instrument. For the optical equivalent diameter of the CAS the refractive index chosen is 1.56, since it is the closest to mineral dust, reported to be 1.59 by Kandler et al. (2007). Due to the low sampling statistics of the PALMS instrument, a 90 seconds time interval was used to calculate the PALMS mineral dust number fraction for the filtered dataset, where the mineral dust number fraction represents the ratio of particles classified as mineral dust to the total number of particles of the filtered data. The CAPS measurements where averaged to match the 90 seconds time interval of the PALMS mineral dust number fraction. The result is visible in Figure 12, where the data including all flights of the ACCLIP field experiment is plotted. It needs to be mentioned, that a high mineral dust fraction does not automatically mean the measurement of many mineral dust particles. For example, a mineral dust fraction of one could also mean, that during the averaged time, in total one particle was measured by PALMS, which was classified as mineral dust. To make this visible, the color code in Figure 12 describes the number of particles measured by PALMS during these 90 seconds.

3.4.2 FLEXPART and FLEXDUST

One of the goals of this work is to identify the potential source regions of the mineral dust measurements. For this, the combination of the models FLEXPART and FLEXDUST will be used.

FLEXPART is a particle dispersion model, developed and described by Stohl et al. (2005): It simulates transport of a particle ensemble over a long-range and mesoscale. FLEXPART further considers dry and wet deposition and diffusion. The model can either be used forward in time, to simulate how particles distribute from a source. Or backward in time, where for a given receptor, potential source contributions are determined.

The setting, needed for the specific use of this study, is a backward simulation. Particles are released from the location of the measurement (receptor point) and the model is used to calculate the location and concentration of the particles backward in time and space. The calculation considers wet and dry deposition and the characteristics of the aerosol species. The version used in this thesis is FLEXPART 11, where the accuracy, efficiency and flexibility were improved by Bakels, Tatsii, et al. (2024) in comparison to the previous version.

FLEXDUST is a model for mineral dust emissions, which incorporates the influence of the meteorological conditions on the emission of mineral dust. This model provides mineral dust emissions as *release files*, containing the number and position of emitted mineral dust particles (Groot Zwaaftink et al., 2016). These files can then be combined with the FLEXPART simulation, resulting in an estimation of mineral dust contribution of different regions at the receptor point.

4 Results

As already established in the methods section and shown in Figure 12, mineral dust was measured during ACCLIP 2022. Hereby, the transfer flights and the first two research flights starting from North America are included, as well as the research flights from Asia. To determine whether and where mineral dust measurements took place in Asia and over the Pacific the flight tracks are plotted in Figure 13 with mineral dust measurements (dust fraction > 0) in blue. In addition, if the number fraction of mineral dust exceeds 0.25 the flight tracks are colored in orange. This shows that mineral dust measurements took place in Asia and over the Pacific.

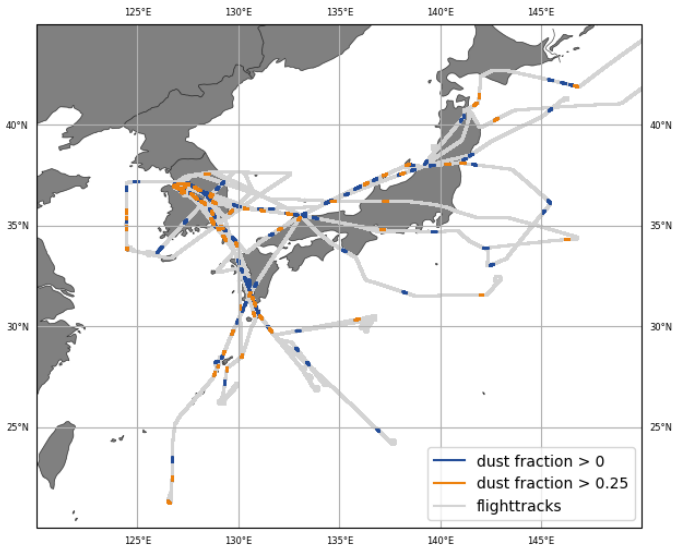

Figure 13: Flight tracks of the research flights in Asia with mineral dust number fraction > 0 in blue and in addition > 0.25 in orange.

To identify periods of mineral dust measurements with enhanced coarse mode aerosol concentrations, a combination of the PALMS and CAS data is used as detection criteria as follows: If the CAS total number concentration shows an increase for a period of time, where PALMS measures mineral dust as well, it is defined as potential period of mineral dust measurement. In the following, such a period of increase of the CAS total number concentration will be called *sequence*.

Following the presented procedure, six sequences could be identified, which are listed in **Fehler! Verweisquelle konnte nicht gefunden werden.**.

Table 4: Identified sequences, including the date, start and stop time and the duration of the potential mineral dust measurement.

name	date	start	stop	duration
sequence 1	20220804	05:40:30	05:42:40	00:02:10
sequence 2	20220804	05:44:20	05:44:37	00:00:17
sequence 3	20220812	07:29:58	07:30:18	00:00:20

sequence 4	20220812	07:30:47	07:31:15	00:00:28
sequence 5	20220823	06:37:02	06:37:38	00:00:36
sequence 6	20220829	02:22:12	02:22:37	00:00:25

Sequence 2 is too short for the analysis. In addition, the nearby presence of clouds is considered, which is the case for sequence 3 and 4. The images of CIP during these periods do also show particles shaped like cloud particles as visible in Figure 14. Therefore, these sequences are excluded from the periods of potential mineral dust measurements.

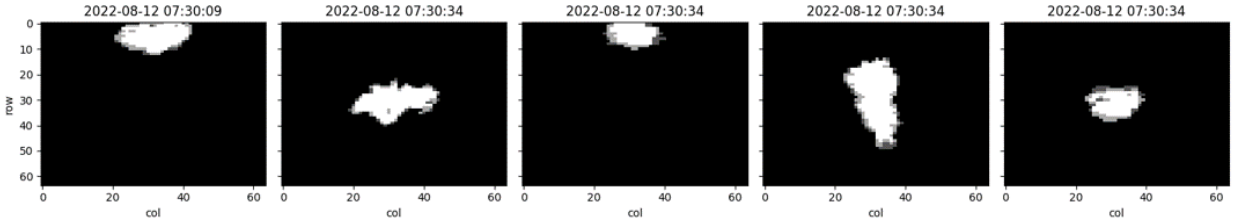

Figure 14: CIP images within sequence 3 to 4. The images show shadows shaped like cloud particles.

Sequence 5 and 6 are also excluded, since within the period of potential mineral dust measurement, the CAS quality flag is greater than zero and therefore filters data. This results in the further analysis of sequence 1, with the hypothesis that here, a mineral *dust layer* was observed.

Additionally, *background* measurements for comparison are chosen that are located before and after the detected sequence. They do not show noticeable features in the CAS total number concentration data and are each one minute long. Furthermore, a third category is introduced called *transition*. This is defined as the increase and decrease of the total number concentration. The decision to exclude these periods of the defined mineral dust measurement is based on the assumption that the mineral dust layer is not isolated from its surroundings. In this case the mineral dust particles mix with the ambient, creating a transition from the background to the mineral dust layer.

The identified mineral dust layer was measured during the RF 04 on August 4th, 2022. In Figure 15 the flight track of RF 04 is pictured with a zoom to the described and analyzed sequence. The measurement took place over the mainland of South Korea and during the descent of the NASA WB-57 high-altitude research aircraft. The airplane flew from south-east to north-west heading towards the Osan Air Base. In Figure 15 the location of the mineral dust layer is pictured in orange and the two background periods in blue.

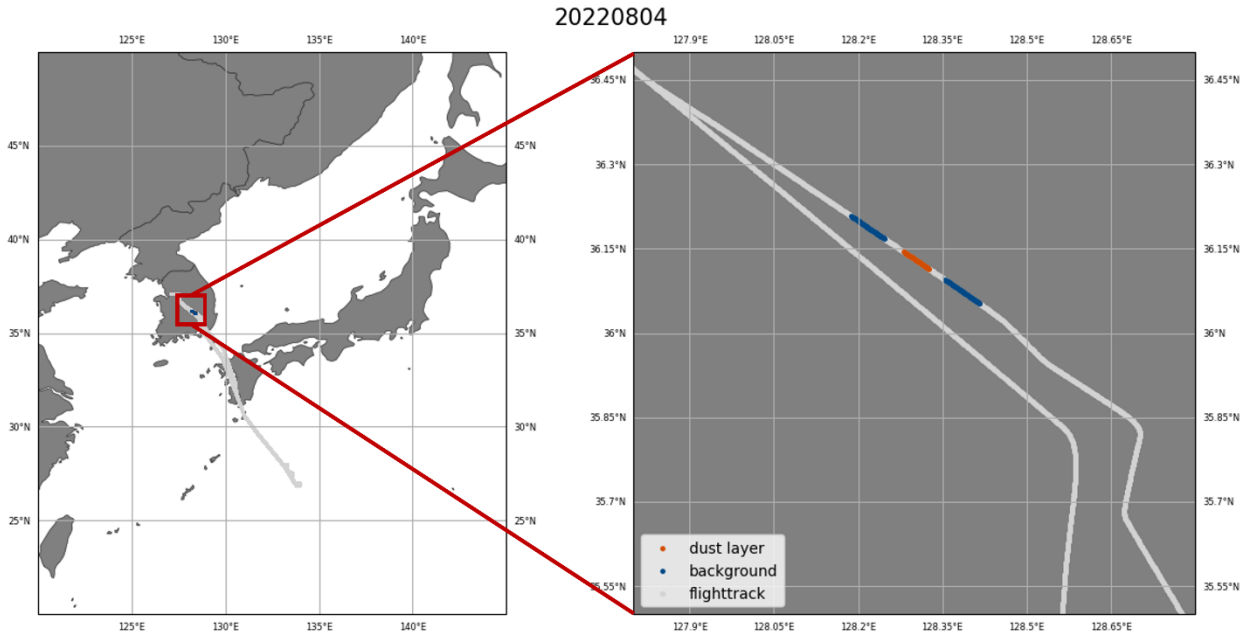

Figure 15: Flight track of RF 04, with zoom to the measurement of the mineral dust layer (orange) and background periods (blue).

Figure 16 shows the time series of median (black line) and in interquartile range (IQR, grey shade) of the total STP number concentration of the CAS, including the mineral dust layer and background periods shaded in orange and blue. The previously introduced transition period is shaded in light blue. Median and IQR are calculated for time intervals of 1 second using the 10 Hz input data. Additionally, the upper panel in Figure 16 indicates the times of PALMS detected mineral dust particles with a diameter of at least 0.5 µm in yellow. The majority of these particles occurred within the defined sequence of increased coarse mode particle number concentrations. However, some of the PALMS mineral dust detections are measured before and after the dust layer during the transition.

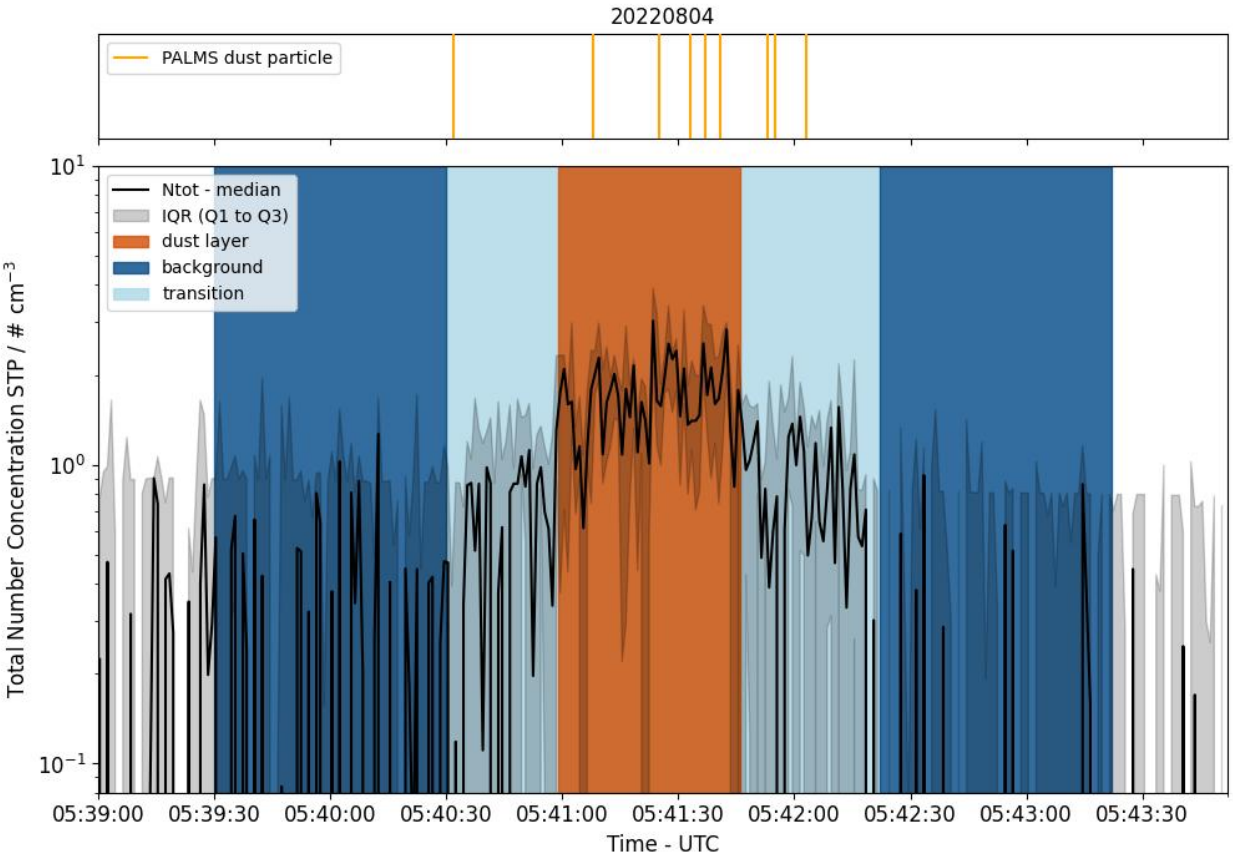

Figure 16: The upper panel shows the time stamps of particles classified as mineral dust by the PALMS, in the bottom plot the time series of total number concentrations at STP of the CAS is shown. The solid black line represents the median values with Q1 to Q3 shaded accordingly. The background is colored in orange for the mineral dust layer, blue for the background and light blue for the transition.

The mineral dust layer was measured between 05:40:59 UTC and 04:41:46 UTC for a duration of 47 seconds. The median total number concentration at STP is 1.67 #/cm³ with IQR of 1.45 to 1.94 #/cm³. In comparison, the background measured a total number concentration at STP of 0.41 #/cm³, which is about 25 % of the concentration measured during the mineral dust layer. For particles larger than 1 µm the concentration within the mineral dust layer is 0.76 #/cm³, whereas the background only shows a concentration of 0.084 #/cm³, which is equal to 11 % of the measurement within the mineral dust layer. The number concentrations and corresponding quartiles are listed in Table 5.

Table 5: Values of the mineral dust layer and background measurement. The total number concentration of the CAS at STP (N_{tot}) and the number concentration of particles > 1 µm (N_{coa}), also measured by the CAS at STP. Additionally, the 25th and 75th percentiles (Q1 and Q3) are included in the table. All values for the number concentrations are given in #/cm³.

Name	Duration	N_{tot} median	N_{tot} Q1	N_{tot} Q2	N_{coa} median	N_{coa} Q1	N_{coa} Q2
Dust layer	47 seconds	1.67	1.35	1.94	0.76	0.49	0.97
Background	2 minutes	0.41	0.31	0.52	0.084	0.016	0.17

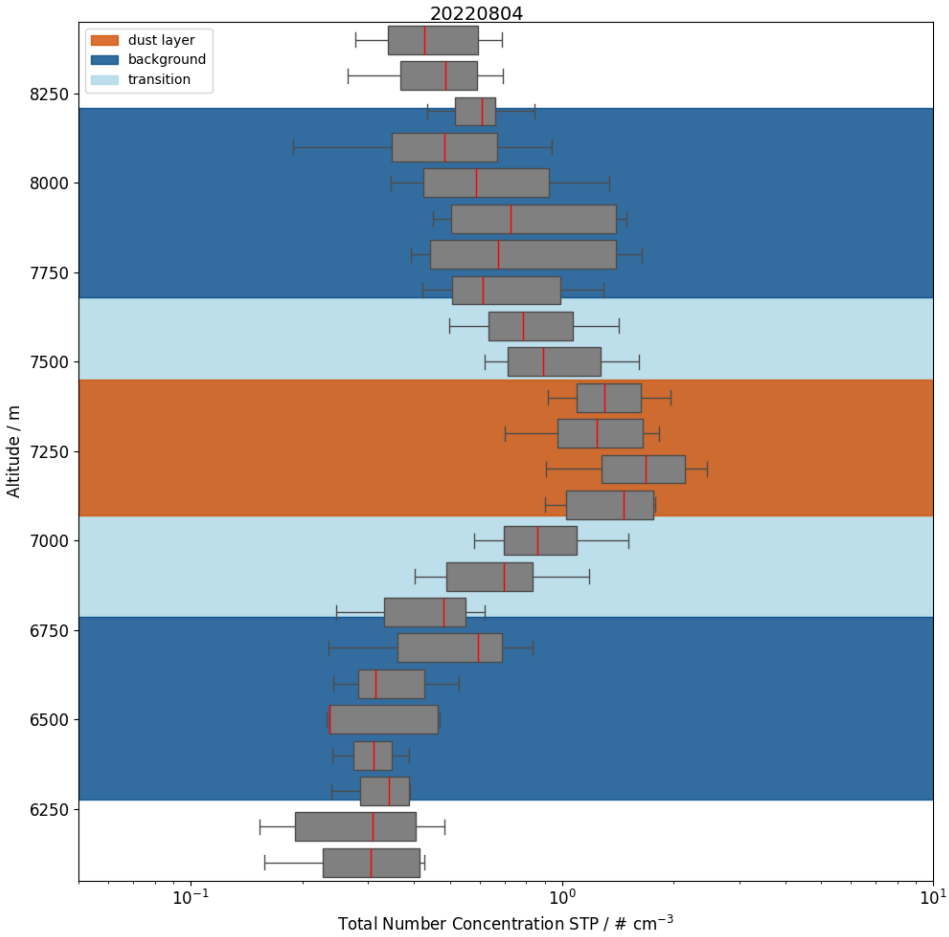

Figure 17: Boxplot of the total number concentration plotted against the height. In red are the median values pictured and the whiskers include 10 to 90 % of the data. The vertical profile is shaded in orange to represent the mineral dust layer, in blue for the background and light blue shows the transition.

Since the measurement took place during the descent of the airplane, the distinct feature of the mineral dust layer is visible in the vertical profile. A boxplot of the CAS total number concentration against the altitude is plotted in Figure 17. For each boxplot element, the median is pictured in red and the whiskers include 10 and 90 % of all data points. The altitude range is binned in 100 m intervals and the shading for mineral dust layer (orange), transition (grey) and background (blue) corresponds to Figure 20.

The mineral dust layer was measured between 7450 m to 7069 m of altitude, therefore the vertical extent is 381 m. The mean altitude of the mineral dust layer is located at a mean altitude of 7264 (± 110) m. The background period above the mineral dust layer spans over 528 m, starting at 8205 m. The background period below the mineral dust layer stretches over 510 m, starting at an altitude of 6785 m.

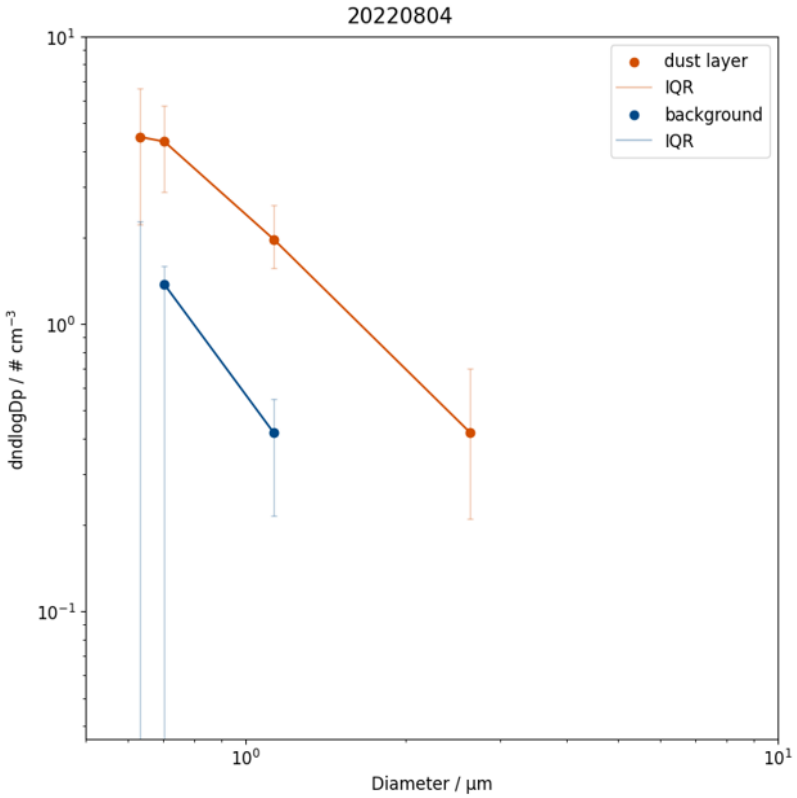

Figure 18: Median values of the number size distributions with IQR as error bars. In orange the values of the mineral dust layer are shown, and in blue the ones of the background.

In Figure 18 the number size distributions of the mineral dust layer (orange) and background (blue) are plotted. It shows the median values as a scatter plot with the 25th and 75th percentiles pictured as error bars. The x-axis displays the mid diameter of the bins, measured by the CAS and both axes are logarithmically displayed.

The lower limit of the y axis is equal to the detection limit of the CAS, which is calculated with the true air speed of the airplane and the resulting measurement volume of the instrument. The detection limit is defined, as one particle within the measurement volume per time unit. For one second and the mean true air speed of 129.7 m/s during the measurement the detection limit results in 0.034 #/cm³.

The size distribution of the mineral dust layer shows the presence of particles with a diameter of greater than 2 µm. The highest median concentration is measured at 0.6 µm with 4.5 #/cm^3. The background case shows lower concentrations with a maximum particle diameter of 1.1 µm and a maximum concentration at a diameter of 0.70 µm with 1.4 #/cm³.

Mineral dust particles play a significant role in cloud formation processes, for which the number of ice nucleating particles is the key parameter besides water content and temperature (Lohmann et al., 2016). The parametrization of DeMott et al. (2010) calculates the amount of ice nucleating particles (INPs) per standard liter:

$$n_{IN}(T_k)=a(273.16 - T_k)^b (n_{aer,0.5})^{(c(273.16-T_k)+d)} \quad (3)$$

In equation (3) $n_{aer,0.5}$ is the number concentration of particles with a diameter of 0.5 µm and above in #/cm³. T_k is the temperature in Kelvin and the experimentally determined constants from DeMott et al. (2010) are a = 0.0000594, b=3.33, c = 0.0264 and d = 0.0033.

For the investigated mineral dust layer, the mean temperature during the measurement is 261.06 (± 0.59) K and the median number concentration is 1.67 #/cm³, with IQR of 1.35 to 1.94 #/cm³. The application of equation (4) results in an INP number concentration of **0.283 (± 0.051) #/L^{-1}**. The error is calculated with the propagation of uncertainty, considering the variability of the temperature and total number concentration within the mineral dust layer.

To determine the potential source regions of the identified mineral dust layer, the combination of the FLEXPART and FLEXDUST simulation is used and shown in Figure 19. The FLEXPART simulation were performed with the online FLEXPART tool (Bakels, Duetsch, et al., 2024) using the settings described in the Appendix C. The simulation was done for monodisperse aerosols for which a size of 1 µm was chosen to represent to mineral dust layer. The assumption of density of the mineral dust particles is based on the estimations of Kandler et al (2011): Particles larger than 1 µm are assumed to have a density of 2.5 g/cm³ and particles smaller

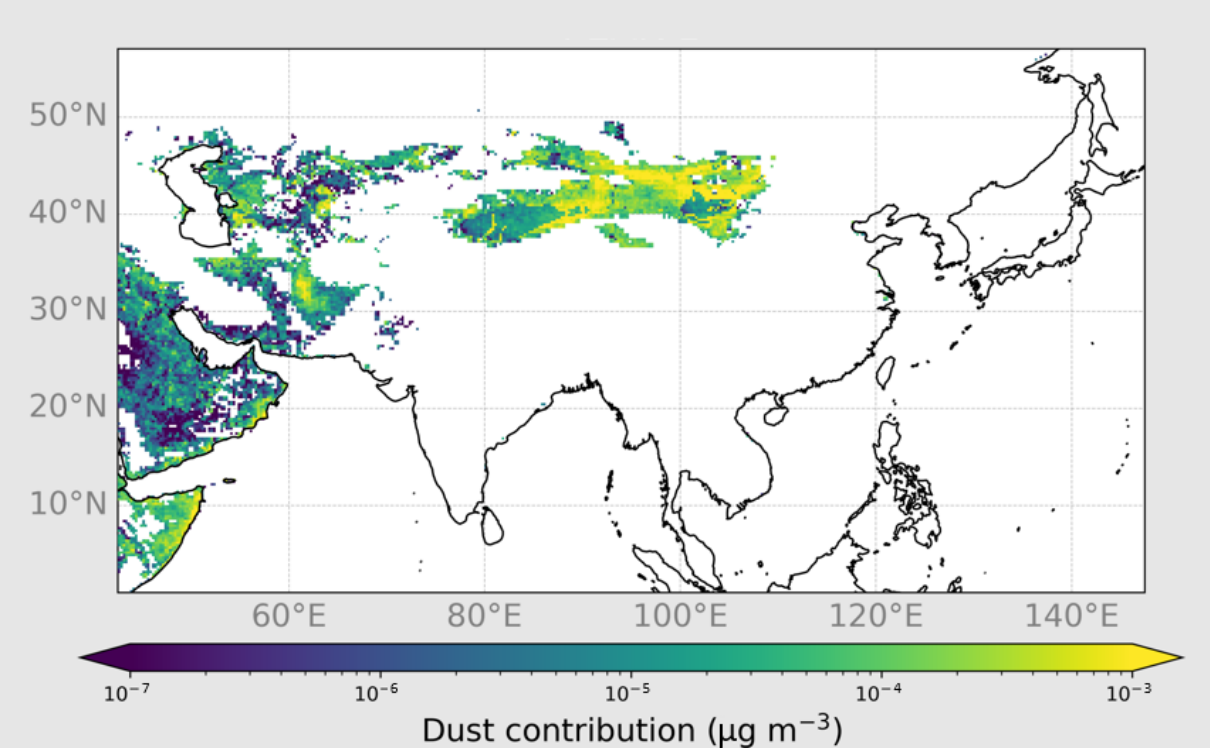

Figure 19: Result of the combination of FLEXDUST and FLEXPART showing the mineral dust contribution of different regions (Acknowledgement to Ioanna Evangelou).

than 1 µm are assigned with a density of 1.5 g/cm³. Therefore, a density of 2 g/cm³ is used for mineral dust particles of 1 µm as used in the simulations performed for this study.

The FLEXDUST simulation and the plot of the mineral dust contribution were provided by Ioanna Evangelou from the University of Vienna's department of meteorology and geophysics. The color code of Figure 19 shows the mass of mineral dust in µg m^{-3} from the different sources to the mineral dust mass of the observed mineral dust layer. The regions of high mineral dust contribution are displayed in yellow, while regions with smaller contribution are colored in a dark violet. The map is roughly bounded to include the Asian mineral dust sources, the region, influenced by the Asian summer monsoon and the location of the research flights during ACCLIP.

In comparison with the Asian mineral dust sources from Figure 1 the highest mineral dust contribution is from regions in Mongolia and north China. The deserts in China contributing are: Qaidam Basin, Kumutage Desert (S5) and Badain Jaran, Tengger Desert, Ulan Buh Desert (S6).

There are smaller contributions of other arid regions further to the west. However, since the FLEXPART simulations are done over a period of 29 days, and within this time span aerosol particles can travel long distances, a temporally resolved analysis would give more insight in future analysis. Nevertheless, the major contributions are clearly from Asian mineral dust sources, which supports the hypothesis, that the mineral dust layer consists of mineral dust originating in Asia.

5 Discussion

The investigation and analysis of the identified mineral dust layer during RF04 shows the measurement of high concentration in coarse mode in comparison with the background as shown in Figure 16 and Figure 17. Additionally, PALMS showed the record of particles classified as mineral dust. The combination of FLEXPART and FLEXDUST indicate the source regions of these mineral dust particles to be the deserts in Mongolia and the north of China.

In this chapter the number size distributions and ice nucleation particle concentration will be discussed in detail.

The number size distribution, displayed in Figure 18, shows the enhanced concentrations for the identified mineral dust layer in comparison with the background measurements. The analysis of the chemical composition of the mineral dust layer confirms furthermore the measurement of mineral dust. In Figure 20 the volume size distribution of particles between 80 nm to 1 µm is displayed, where the colors represent the different aerosol types measured with the PALMS instrument. The figure was provided by Gregory Schill, principal investigator for the PALMS instrument during ACCLIP, and uses the UHSAS (Ultra-High Sensitivity Aerosol Spectrometer) data for the volume distribution where the PALMS composition data is mapped on.

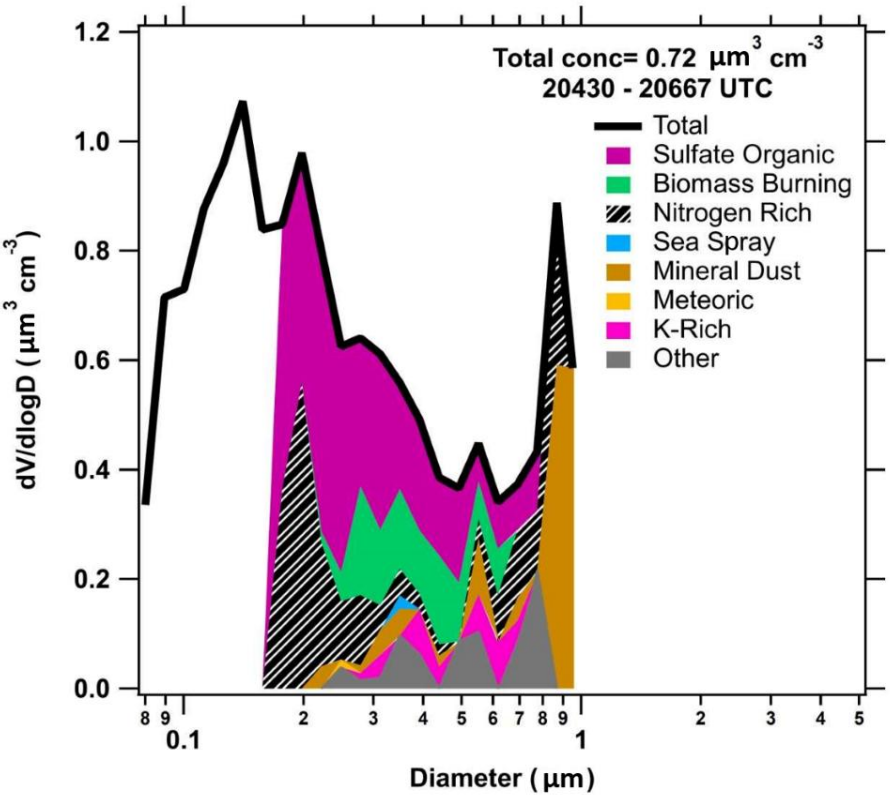

Figure 20: Volume size distribution with palms data mapped on it (Acknowledgment to Gregory Schill). In brown mineral dust is displayed, being the dominant aerosol type for particles larger than 0.8 µm.

The volume size distribution represents a period of about four minutes between 05:40:30 and 04:44:27 UTC where within this time period, the identified mineral dust layer was measured. For particles larger than 0.8 µm mineral dust (brown) is the dominating component of measured aerosol particles. For a diameter of 0.9 µm about 67 % and for 1 µm all measured particles are classified as mineral dust. Besides mineral dust, nitrogen rich aerosol particles where present, as well as other particles, not matching any category of PALMS. Due to size range limitations of the relevant instruments the composition resolved size distributions end at a diameter of 1 µm. However, assuming that the composition for particles larger than 1 µm is comparable to the particles between 0.8 and 1 µm the composition resolved volume size distribution provides good evidence, that the majority of the coarse mode particles in the investigated layer is mineral dust.

The investigated mineral dust layer shows distinct increase in number concentration and therefore can be clearly distinguished from the background. As visible in Figure 16, the median total number concentration increases from 0.4 cm^{-3} for the background period to 1.7 cm^{-3} in the mineral dust layer, which is more than a factor of 4. For particles larger than 1 µm the concentration increases by a factor of 9. The number size distribution, as shown in Figure 18, confirms that not only an increased concentration but also larger particles are measured within the mineral dust layer in comparison to the background period. This behavior is as expected of mineral dust layers and is also shown by various studies (Ardon-Dryer & Kelley, 2022; Shao & Mao, 2016).

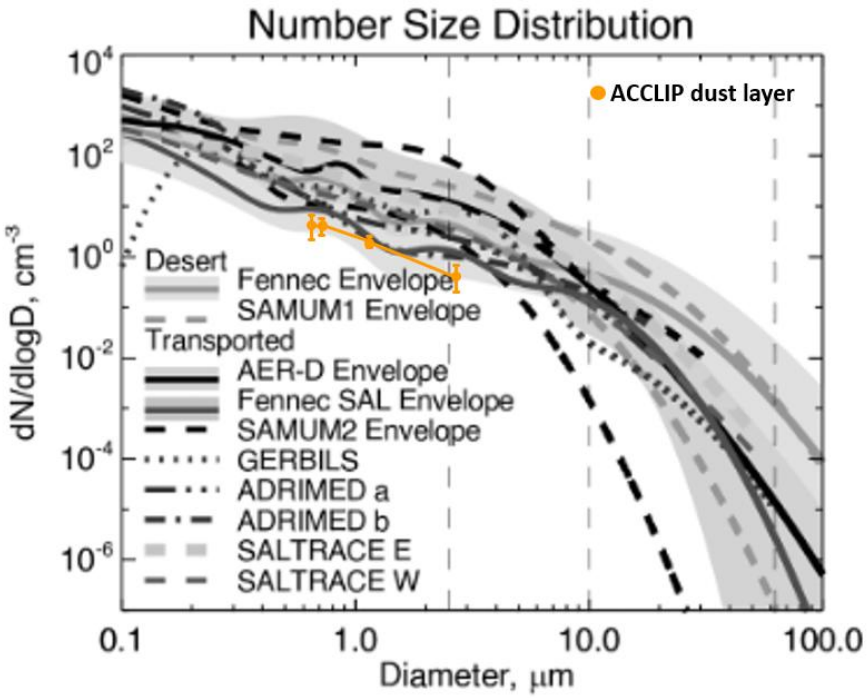

Figure 21: Number size distribution of mineral dust aerosols measurements of different field experiments, including the number size distribution of the mineral dust layer measured during ACCLIP added in orange (adapted form Adebiyi et al. (2023))

Adebiyi et al. (2023) compared particle number size distributions from different campaigns, which took place between 2006 and 2015. Most of them measured transported mineral dust, while two (Fennec Envelope and SAMUM1 Envelope) measured size distributions close to the source. The measurements close to the source show a higher concentration in the super coarse mode but other than that match with the measurements of transported mineral dust within the variability. The number size distribution of the mineral dust layer measured during ACCLIP, which is shown in Figure 24 in orange, matches with the other mineral dust events presented by Adebiyi et al. (2023). The measurement of the ACCLIP mineral dust layer is located at the lower end of the concentrations reported in Adebiyi et al. (2023). The majority of the mineral dust measurements took place between 2 and 5 km of height and at a maximum altitude of 6 km. Therefore, the location in altitude of the ACCLIP mineral dust layer is at least 1 km higher, which may be a reason, why the concentration is at the lower end of the reported number size distribution.

The mineral dust layer during ACCLIP shows particles up to 2.64 µm, therefore the majority of particles measured are within the fine mineral dust regime, as defined previously by Adebiyi et al. (2023) and visualized by the first vertical dashed line in Figure 21. The detection limit of the CAS during the measurement of the mineral dust layer is calculated to be 0.034 #/cm³. The compared number size distributions in Figure 21 show concentrations of below 0.03 #/cm³ from a diameter of 6 µm on. From which can be concluded that even if larger particles where present during the ACCLIP mineral dust layer the concentration of the compared mineral dust measurements are lower than the detection limit of the CAS.

Fine mineral dust particles produce a negative net direct radiative effect, leading to a cooling effect. This is a result of the extinction of short-wave radiation, by mainly scattering light and therefore the particles only absorb a small percentage (Adebiyi et al., 2023). Since the particles measured during the mineral dust layer are mostly within the fine mineral dust mode, it can be assumed, they scatter most of the incoming solar radiation.

Besides interacting directly with radiation, mineral dust has very good ice nucleation properties, which is shown in a study by Chen et al. (2021), where 14 different mineral dust measurements were used to investigate the ability of mineral dust to act as INPs. The resulting INP concentrations is shown as the function of temperature in Figure 22. INP concentrations per standard liter were determined to be within the range of 10^{-2} to 10^{2} at temperatures between -25 to -5 °C. The calculated INP concentration of the analyzed mineral dust layer, measured during ACCLIP, is 0.283 (± 0.051) #/L^{-1} and corresponds to a mean temperature of -13°C during the observation. Figure 26 represents these results in orange. The calculated INP concentration of this study in comparison with the ones measured by Chen et al. (2021) (visualized in grey) do agree as follows: For the mean temperature during the mineral dust layer of -13 °C, the values for the INP concentration in Chen et al. (2021) varies over two magnitudes from 0.1 to 10 INP per standard liter, which well covers the calculated INP concentration of the observed mineral dust layer during ACCLIP. The light blue circles do represent a non-dust day and differ from the other measurements. Showing a one order of magnitude smaller concentrations of INP.

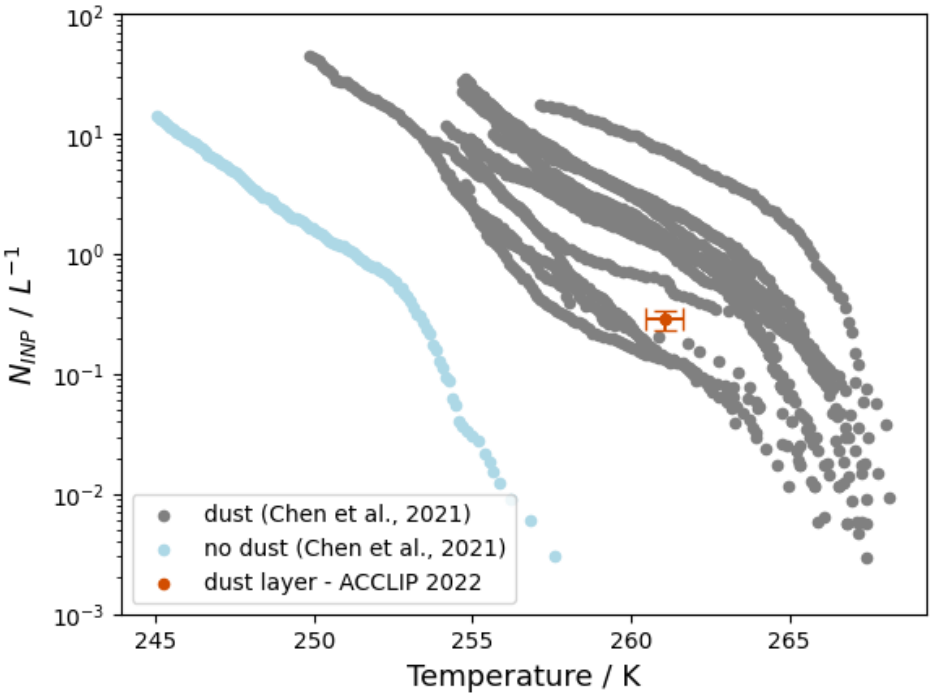

Figure 22: Measured INP concentrations (N_{INP}) plotted as a function of temperature, including the calculated N_{INP} of the analyzed mineral dust layer measured during ACCLIP marked as a yellow cross (adapted from Chen et al. (2021)).

As already described, mineral dust particles in the atmosphere are crucial for cloud formation at temperatures between 0 °C and -38 °C, by acting as INP. Therefore, the measured dust layer, and the resulting INP concentration, has a potential influence on the development and preexisting mixed-phase clouds.

6 Conclusion

In this study a mineral dust layer, measured during the ACCLIP field experiment, was analyzed. As a first step, the ACCLIP data were processed. This included the development of a modified cloud flag suitable for the ACCLIP campaign and the time synchronization of the CAPS data with the other campaign instruments to ensure a qualitative analysis. The ACCLIP data were analyzed, potential time periods in mineral dust layers were determined, and an Asian mineral dust layer was identified utilizing CAS number concentration in combination with PALMS chemical composition measurements. On RF04 on the 4th of August, 2022, between 05:40:59 and 05:41:46 UTC, an Asian dust layer was identified which was characterized in detail. The measurement took place during the descent of the NASA WB-57 high-altitude research aircraft between an altitude of 7450 and 7069 m. For the analysis of this dust layer, the total number concentration, vertical profile, number size distribution, and ice nucleating particle concentration were investigated.

The number size distribution of the dust layer's median values shows enhanced concentrations when compared to the background. Particles up to 2.6 µm were measured within the dust layer, meaning that the majority of these mineral dust particles are defined as fine dust, according to the definition of Adebiyi et al. (2023). Additionally, fine mineral dust particles scatter most of the incoming solar radiation, which may lead to a negative net direct radiative effect, resulting in cooling (Adebiyi et al., 2023). The comparison of the number size distribution of the mineral dust layer measured during ACCLIP agrees with mineral dust observations of various field experiments. The measured concentrations of the mineral dust layer during ACCLIP are on the lower limit of the mineral dust size distributions reported by Adebiyi et al. (2023).

Mineral dust particles show ideal characteristics for acting as INP, and the altitude of measurement and temperature are favorable for mixed-phase clouds. Therefore, the abundance of INPs was analyzed by calculating the concentration of INPs with the parametrization of DeMott et al. (2010), resulting in 0.283 (± 0.051) #/L^{-1}. The comparison of temperature depended measurements of INP concentrations in Asia with the calculations for the dust layer during ACCLIP falls into the range reported by Chen et al. (2021).

With the combination of the particle dispersion model FLEXPART and FLEXDUST, a model for dust emission, the regions of dust contribution were determined. The deserts in Mongolia and the north of China were identified as the main sources of the Asian mineral dust particles measured within the dust layer.

In this thesis one mineral dust layer, identified during the aircraft-based campaign ACCLIP conducted 2022, was analyzed in detail. To better understand mineral dust transported from Asian mineral dust sources by the Asian summer monsoon to the reported altitudes, more measurements are needed. These would give an insight on the variability of the characteristics of these mineral dust aerosols. As well as the influence on cloud formation processes and

earth's radiation budget of these mineral dust particles should be studied. Additionally, measurements of dust influenced clouds are needed to evaluate the influence of mineral dust on clouds.

7 Bibliography

Adebiyi, A., Kok, J. F., Murray, B. J., Ryder, C. L., Stuut, J.-B. W., Kahn, R. A., Knippertz, P., Formenti, P., Mahowald, N. M., Pérez García-Pando, C., Klose, M., Ansmann, A., Samset, B. H., Ito, A., Balkanski, Y., Di Biagio, C., Romanias, M. N., Huang, Y., & Meng, J. (2023). A review of coarse mineral dust in the Earth system. *Aeolian Research*, *60*, 100849. https://doi.org/10.1016/j.aeolia.2022.100849

Aknan, A. (2024, September 24). *NASA Airborne Science Data for Atmospheric Composition* [ACCLIP Data Archive]. https://www-air.larc.nasa.gov/cgi-bin/ArcView/acclip

Ardon-Dryer, K., & Kelley, M. C. (2022). Particle size distribution and particulate matter concentrations during synoptic and convective dust events in West Texas. *Atmospheric Chemistry and Physics*, *22*(13), 9161–9173. https://doi.org/10.5194/acp-22-9161-2022

Bakels, L., Duetsch, M., Tatsii, D., Tipka, A., Seibert, P., Thompson, R., Blaschek, M., Plach, A., Bucci, S., Vojta, M., Cassiani, M., Henne, S., Marie D., M., Maurer, C., Lechner, V., Eckhardt, S., Groot-Zwaaftink, C., Kaufmann, P., Baier, K., … Stohl, A. (2024). *FLEXPART-v11* (Version 2c095d0f). Zenodo. https://doi.org/10.5281/ZENODO.12706632

Bakels, L., Tatsii, D., Tipka, A., Thompson, R., Dütsch, M., Blaschek, M., Seibert, P., Baier, K., Bucci, S., Cassiani, M., Eckhardt, S., Groot Zwaaftink, C., Henne, S., Kaufmann, P., Lechner, V., Maurer, C., Mulder, M. D., Pisso, I., Plach, A., … Stohl, A. (2024). FLEXPART version 11: Improved accuracy, efficiency, and flexibility. *Geoscientific Model Development*, *17*(21), 7595–7627. https://doi.org/10.5194/gmd-17-7595-2024

Baumgardner, D., Jonsson, H., Dawson, W., O'Connor, D., & Newton, R. (2001). The cloud, aerosol and precipitation spectrometer: A new instrument for cloud investigations. *Atmospheric Research*, *59–60*, 251–264. https://doi.org/10.1016/S0169-8095(01)00119-3

Bergman, J. W., Fierli, F., Jensen, E. J., Honomichl, S., & Pan, L. L. (2013). Boundary layer sources for the Asian anticyclone: Regional contributions to a vertical conduit. *Journal of Geophysical Research: Atmospheres*, *118*(6), 2560–2575. https://doi.org/10.1002/jgrd.50142

Bolin, B., Aspling, G., & Persson, C. (1974). Residence time of atmospheric pollutants as dependent on source characteristics, atmospheric diffussion processes and sink mechanisms. *Tellus*, *26*(1–2), 185–195. https://doi.org/10.1111/j.2153-3490.1974.tb01966.x

Bossolasco, A., Jegou, F., Sellitto, P., Berthet, G., Kloss, C., & Legras, B. (2021). Global modeling studies of composition and decadal trends of the Asian Tropopause Aerosol Layer. *Atmospheric Chemistry and Physics*, *21*(4), 2745–2764. https://doi.org/10.5194/acp-21-2745-2021

Boucher, O. (2015). *Atmospheric Aerosols*. Springer Netherlands. https://doi.org/10.1007/978-94-017-9649-1

Chen, J., Wu, Z., Chen, J., Reicher, N., Fang, X., Rudich, Y., & Hu, M. (2021). Size-resolved atmospheric ice-nucleating particles during East Asian dust events. *Atmospheric Chemistry and Physics*, *21*(5), 3491–3506. https://doi.org/10.5194/acp-21-3491-2021

Choobari, O. A., Zawar-Reza, P., & Sturman, A. (2014). The global distribution of mineral dust and its impacts on the climate system: A review. *Atmospheric Research*, *138*, 152–165. https://doi.org/10.1016/j.atmosres.2013.11.007

Cziczo, D. J., Froyd, K. D., Hoose, C., Jensen, E. J., Diao, M., Zondlo, M. A., Smith, J. B., Twohy, C. H., & Murphy, D. M. (2013). Clarifying the Dominant Sources and Mechanisms of Cirrus Cloud Formation. *Science*, *340*(6138), 1320–1324. https://doi.org/10.1126/science.1234145

DeMott, P. J., Prenni, A. J., Liu, X., Kreidenweis, S. M., Petters, M. D., Twohy, C. H., Richardson, M. S., Eidhammer, T., & Rogers, D. C. (2010). Predicting global atmospheric ice nuclei distributions and their impacts on climate. *Proceedings of the National Academy of Sciences*, *107*(25), 11217–11222. https://doi.org/10.1073/pnas.0910818107

Diskin, G. S., Podolske, J. R., Sachse, G. W., & Slate, T. A. (2002). *Open-path airborne tunable diode laser hygrometer* (A. Fried, Ed.; p. 196). https://doi.org/10.1117/12.453736

Dollner, M. (2022). *Assessment of the global distribution of coarse-mode aerosol and clouds with large-scale in situ aircraft observations*. https://doi.org/10.25365/THESIS.72087

Dollner, M., Gasteiger, J., Schöberl, M., Gattringer, A., Beres, N. D., Bui, T. P., Diskin, G., & Weinzierl, B. (2024). The Cloud Indicator: A novel algorithm for automatic detection and classification of clouds using airborne in situ observations. *Atmospheric Research*, *308*, 107504. https://doi.org/10.1016/j.atmosres.2024.107504

Froyd, K. D., Yu, P., Schill, G. P., Brock, C. A., Kupc, A., Williamson, C. J., Jensen, E. J., Ray, E., Rosenlof, K. H., Bian, H., Darmenov, A. S., Colarco, P. R., Diskin, G. S., Bui, T., & Murphy, D. M. (2022). Dominant role of mineral dust in cirrus cloud formation revealed by global-scale measurements. *Nature Geoscience*, *15*(3), 177–183. https://doi.org/10.1038/s41561-022-00901-w

Gettelman, A., Hoor, P., Pan, L. L., Randel, W. J., Hegglin, M. I., & Birner, T. (2011). THE EXTRATROPICAL UPPER TROPOSPHERE AND LOWER STRATOSPHERE. *Reviews of Geophysics*, *49*(3), 2011RG000355. https://doi.org/10.1029/2011RG000355

Gill, A. E. (1980). Some simple solutions for heat-induced tropical circulation. *Quarterly Journal of the Royal Meteorological Society*, *106*(449), 447–462. https://doi.org/10.1002/qj.49710644905

Gottschaldt, K. D., Schlager, H., Baumann, R., Bozem, H., Eyring, V., Hoor, P., Jöckel, P., Jurkat, T., Voigt, C., Zahn, A., & Ziereis, H. (2017). Trace gas composition in the Asian summer monsoon anticyclone: A case study based on aircraft observations and model simulations. *Atmospheric Chemistry and Physics*, *17*(9), 6091–6111. https://doi.org/10.5194/acp-17-6091-2017

Groot Zwaaftink, C. D., Grythe, H., Skov, H., & Stohl, A. (2016). Substantial contribution of northern high-latitude sources to mineral dust in the Arctic. *Journal of Geophysical Research: Atmospheres*, *121*(22). https://doi.org/10.1002/2016JD025482

Highwood, E. J., & Hoskins, B. J. (1998). The tropical tropopause. *Quarterly Journal of the Royal Meteorological Society*, *124*(549), 1579–1604. https://doi.org/10.1002/qj.49712454911

Hinds, W. C. (1999). *Aerosol technology: Properties, behavior, and measurement of airborne particles* (2nd ed.). John Wiley & Sons, Incorporated.

Holton, J. R. (2004). *An introduction to dynamic meteorology* (4th ed.). Elsevier,.

Honomichl, S. B., & Pan, L. L. (2020). Transport From the Asian Summer Monsoon Anticyclone Over the Western Pacific. *Journal of Geophysical Research: Atmospheres*, *125*(13), e2019JD032094. https://doi.org/10.1029/2019JD032094

Hoskins, B. J., & Rodwell, M. J. (1995). A Model of the Asian Summer Monsoon. Part I: The Global Scale. *Journal of the Atmospheric Sciences*, *52*(9), 1329–1340. https://doi.org/10.1175/1520-0469(1995)052<1329:AMOTAS>2.0.CO;2

Huang, Y., Adebiyi, A. A., Formenti, P., & Kok, J. F. (2021). Linking the Different Diameter Types of Aspherical Desert Dust Indicates That Models Underestimate Coarse Dust Emission. *Geophysical Research Letters*, *48*(6), e2020GL092054. https://doi.org/10.1029/2020GL092054

Intergovernmental Panel On Climate Change (Ed.). (2014). *Climate Change 2013 – The Physical Science Basis: Working Group I Contribution to the Fifth Assessment Report of the Intergovernmental Panel on Climate Change* (1st ed.). Cambridge University Press. https://doi.org/10.1017/CBO9781107415324

Kandler, K., Benker, N., Bundke, U., Cuevas, E., Ebert, M., Knippertz, P., Rodríguez, S., Schütz, L., & Weinbruch, S. (2007). Chemical composition and complex refractive index of Saharan Mineral Dust at Izaña, Tenerife (Spain) derived by electron microscopy. *Atmospheric Environment*, *41*(37), 8058–8074. https://doi.org/10.1016/j.atmosenv.2007.06.047

Kandler, K., Schütz, L., Jäckel, S., Lieke, K., Emmel, C., Müller-Ebert, D., Ebert, M., Scheuvens, D., Schladitz, A., Šegvić, B., Wiedensohler, A., & Weinbruch, S. (2011). Ground-based off-line aerosol measurements at Praia, Cape Verde, during the Saharan Mineral Dust Experiment: Microphysical properties and mineralogy. *Tellus B: Chemical and Physical Meteorology*, *63*(4), 459. https://doi.org/10.1111/j.1600-0889.2011.00546.x

Kok, J. F., Storelvmo, T., Karydis, V. A., Adebiyi, A. A., Mahowald, N. M., Evan, A. T., He, C., & Leung, D. M. (2023). Mineral dust aerosol impacts on global climate and climate change. *Nature Reviews Earth & Environment*, *4*(2), 71–86. https://doi.org/10.1038/s43017-022-00379-5

Kulkarni, P., Baron, P. A., & Willeke, K. (Eds.). (2011). *Aerosol Measurement: Principles, Techniques, and Applications* (1st ed.). Wiley. https://doi.org/10.1002/9781118001684

Lohmann, U., Lüönd, F., & Mahrt, F. (2016). *An Introduction to Clouds: From the Microscale to Climate* (1st ed.). Cambridge University Press. https://doi.org/10.1017/CBO9781139087513

Ma, J., Brühl, C., He, Q., Steil, B., Karydis, V. A., Klingmüller, K., Tost, H., Chen, B., Jin, Y., Liu, N., Xu, X., Yan, P., Zhou, X., Abdelrahman, K., Pozzer, A., & Lelieveld, J. (2019). Modeling the aerosol chemical composition of the tropopause over the Tibetan Plateau during the Asian summer monsoon. *Atmospheric Chemistry and Physics*, *19*(17), 11587–11612. https://doi.org/10.5194/acp-19-11587-2019

Murphy, D. M., & Koop, T. (2005). Review of the vapour pressures of ice and supercooled water for atmospheric applications. *Quarterly Journal of the Royal Meteorological Society*, *131*(608), 1539–1565. https://doi.org/10.1256/qj.04.94

Murphy, D. M., & Thomson, D. S. (1995). Laser Ionization Mass Spectroscopy of Single Aerosol Particles. *Aerosol Science and Technology*, *22*(3), 237–249. https://doi.org/10.1080/02786829408959743

Pan, L. L., Atlas, E. L., Honomichl, S. B., Smith, W. P., Kinnison, D. E., Solomon, S., Santee, M. L., Saiz-Lopez, A., Laube, J. C., Wang, B., Ueyama, R., Bresch, J. F., Hornbrook, R. S., Apel, E. C., Hills, A. J., Treadaway, V., Smith, K., Schauffler, S., Donnelly, S., … Newman, P. A. (2024). East Asian summer monsoon delivers large abundances of very short-lived organic chlorine substances to the lower stratosphere. *Proceedings of the National Academy of Sciences*, *121*(12), e2318716121. https://doi.org/10.1073/pnas.2318716121

Pan, L. L., Honomichl, S. B., Kinnison, D. E., Abalos, M., Randel, W. J., Bergman, J. W., & Bian, J. (2016). Transport of chemical tracers from the boundary layer to stratosphere associated with the dynamics of the Asian summer monsoon. *Journal of Geophysical Research: Atmospheres*, *121*(23). https://doi.org/10.1002/2016JD025616

Randel, W. J., & Park, M. (2006). Deep convective influence on the Asian summer monsoon anticyclone and associated tracer variability observed with Atmospheric Infrared

Sounder (AIRS). *Journal of Geophysical Research: Atmospheres*, *111*(D12), 2005JD006490. https://doi.org/10.1029/2005JD006490

Riemer, N., Ault, A. P., West, M., Craig, R. L., & Curtis, J. H. (2019). Aerosol Mixing State: Measurements, Modeling, and Impacts. *Reviews of Geophysics*, *57*(2), 187–249. https://doi.org/10.1029/2018RG000615

Roedel, W., & Wagner, T. (2017). *Physik unserer Umwelt: Die Atmosphäre* (5. Auflage). Springer Spektrum.

Sarkozy, L. C., Clouser, B. W., Lamb, K. D., Stutz, E. J., Saathoff, H., Möhler, O., Ebert, V., & Moyer, E. J. (2020). The Chicago Water Isotope Spectrometer (ChiWIS-lab): A tunable diode laser spectrometer for chamber-based measurements of water vapor isotopic evolution during cirrus formation. *Review of Scientific Instruments*, *91*(4), 045120. https://doi.org/10.1063/1.5139244

Schepanski, K. (2018). Transport of Mineral Dust and Its Impact on Climate. *Geosciences*, *8*(5), 151. https://doi.org/10.3390/geosciences8050151

Scott, S. G., Bui, T. P., Chan, K. R., & Bowen, S. W. (1990). The Meteorological Measurement System on the NASA ER-2 Aircraft. *Journal of Atmospheric and Oceanic Technology*, *7*(4), 525–540. https://doi.org/10.1175/1520-0426(1990)007<0525:TMMSOT>2.0.CO;2

Seinfeld, J. H., & Pandis, S. N. (2016). *Atmospheric chemistry and physics: From air pollution to climate change* (Third edition). John Wiley & Sons.

Shao, J., & Mao, J. (2016). Dust Particle Size Distributions during Spring in Yinchuan, China. *Advances in Meteorology*, *2016*, 1–8. https://doi.org/10.1155/2016/6940502

Stanelle, T., Bey, I., Raddatz, T., Reick, C., & Tegen, I. (2014). Anthropogenically induced changes in twentieth century mineral dust burden and the associated impact on radiative

forcing. *Journal of Geophysical Research: Atmospheres*, *119*(23). https://doi.org/10.1002/2014JD022062

Stohl, A., Forster, C., Frank, A., Seibert, P., & Wotawa, G. (2005). Technical note: The Lagrangian particle dispersion model FLEXPART version 6.2. *Atmos. Chem. Phys.*

Thomson, D. S., Schein, M. E., & Murphy, D. M. (2000). Particle Analysis by Laser Mass Spectrometry WB-57F Instrument Overview. *Aerosol Science and Technology*, *33*(1–2), 153–169. https://doi.org/10.1080/027868200410903

UCAR. (2024, September 23). *Asian Summer Monsoon Chemical and Climate Impact Project*. https://www2.acom.ucar.edu/acclip

Vali, G., DeMott, P. J., Möhler, O., & Whale, T. F. (2015). Technical Note: A proposal for ice nucleation terminology. *Atmospheric Chemistry and Physics*, *15*(18), 10263–10270. https://doi.org/10.5194/acp-15-10263-2015

Weinzierl, B., Ansmann, A., Prospero, J. M., Althausen, D., Benker, N., Chouza, F., Dollner, M., Farrell, D., Fomba, W. K., Freudenthaler, V., Gasteiger, J., Groß, S., Haarig, M., Heinold, B., Kandler, K., Kristensen, T. B., Mayol-Bracero, O. L., Müller, T., Reitebuch, O., … Walser, A. (2017). The Saharan Aerosol Long-Range Transport and Aerosol–Cloud-Interaction Experiment: Overview and Selected Highlights. *Bulletin of the American Meteorological Society*, *98*(7), 1427–1451. https://doi.org/10.1175/BAMS-D-15-00142.1

Xu, C., Ma, Y. M., You, C., & Zhu, Z. K. (2015). The regional distribution characteristics of aerosol optical depth over the Tibetan Plateau. *Atmospheric Chemistry and Physics*, *15*(20), 12065–12078. https://doi.org/10.5194/acp-15-12065-2015

Yihui, D., & Chan, J. C. L. (2005). The East Asian summer monsoon: An overview. *Meteorology and Atmospheric Physics*, *89*(1–4), 117–142. https://doi.org/10.1007/s00703-005-0125-z

Yu, P., Rosenlof, K. H., Liu, S., Telg, H., Thornberry, T. D., Rollins, A. W., Portmann, R. W., Bai, Z., Ray, E. A., Duan, Y., Pan, L. L., Toon, O. B., Bian, J., & Gao, R.-S. (2017). Efficient transport of tropospheric aerosol into the stratosphere via the Asian summer monsoon anticyclone. *Proceedings of the National Academy of Sciences*, *114*(27), 6972–6977. https://doi.org/10.1073/pnas.1701170114

Zhang, X. Y., Gong, S. L., Zhao, T. L., Arimoto, R., Wang, Y. Q., & Zhou, Z. J. (2003). Sources of Asian dust and role of climate change versus desertification in Asian dust emission. *Geophysical Research Letters*, *30*(24), 2003GL018206. https://doi.org/10.1029/2003GL018206

Zimmermann, F., Weinbruch, S., Schütz, L., Hofmann, H., Ebert, M., Kandler, K., & Worringen, A. (2008). Ice nucleation properties of the most abundant mineral dust phases. *Journal of Geophysical Research: Atmospheres*, *113*(D23), 2008JD010655. https://doi.org/10.1029/2008JD010655

Appendix

A. Cloudflag approach with ChiWIS Data

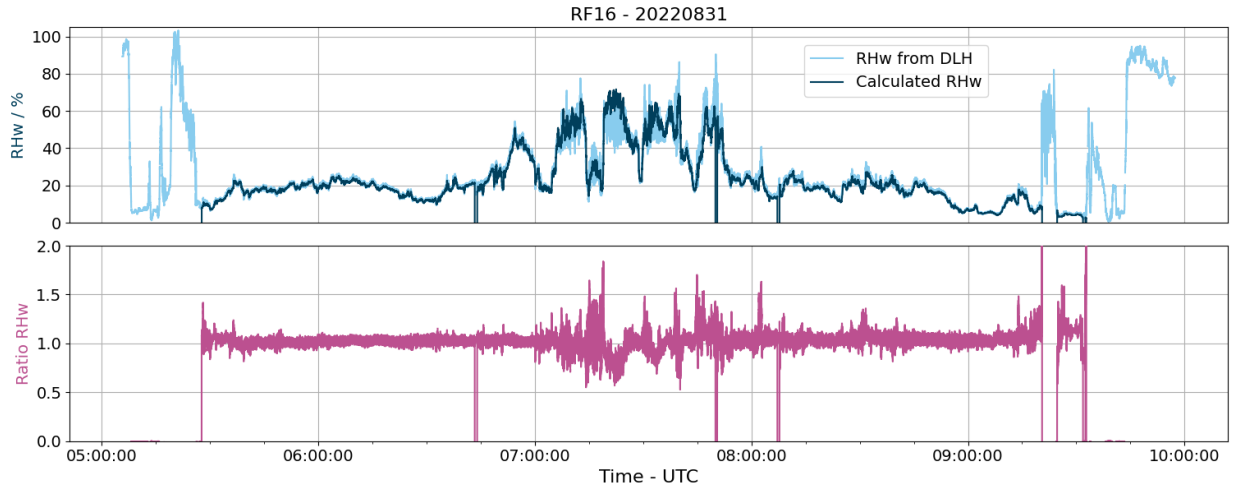

Figure 23: Relative humidity in respect to water: in light blue the provided data of DLH and dark blue the calculated values using ChiWIS data. The bottom plot shows the ratio of the calculated RH_w to the RH_w of DLH.

To validate this, the calculation is done for a randomly selected flight (RF16 on August 31st 2022), where data from the DLH is available. Then the calculated new approach is compared to the cloud flag of Dollner et al. (2024).

The ChiWIS instrument provides H_2O data, which was used to calculate the relative humidity applying the calculation method as described by Murphy & Koop (2005). To validate the new approach, relative humidity obtained from the ChiWIS data was compared to the data from DLH for the RF16 (20220831), where both instruments were operational. The result is plotted in Figure 23 Since ChiWIS provides one measurement every 5 seconds fast response to changes in relative humidity cannot be identified. This is visible in the ratio between the provided RH_w of DLH and the calculated RH_w using ChiWIS data, plotted Figure 23 in the bottom. Rapid changes in relative humidity, well captured by the DLH instrument are not represented by the ChiWIS relative humidity, visible in the large deflections of the ratio. Furthermore, the ratio shows strong deviations of up to 50 % when the DLH data shows high variation. In addition, the measurement limitations of ChiWIS are reached when the aircraft is ascending and descending. Hence no calculation of RHw can be done here. Due to the discussed limitation of this method, it is not suitable to use ChiWIS data for the cloud flag for the ACCLIP campaign.

B. Timeseries of sequences of potential dust measurements

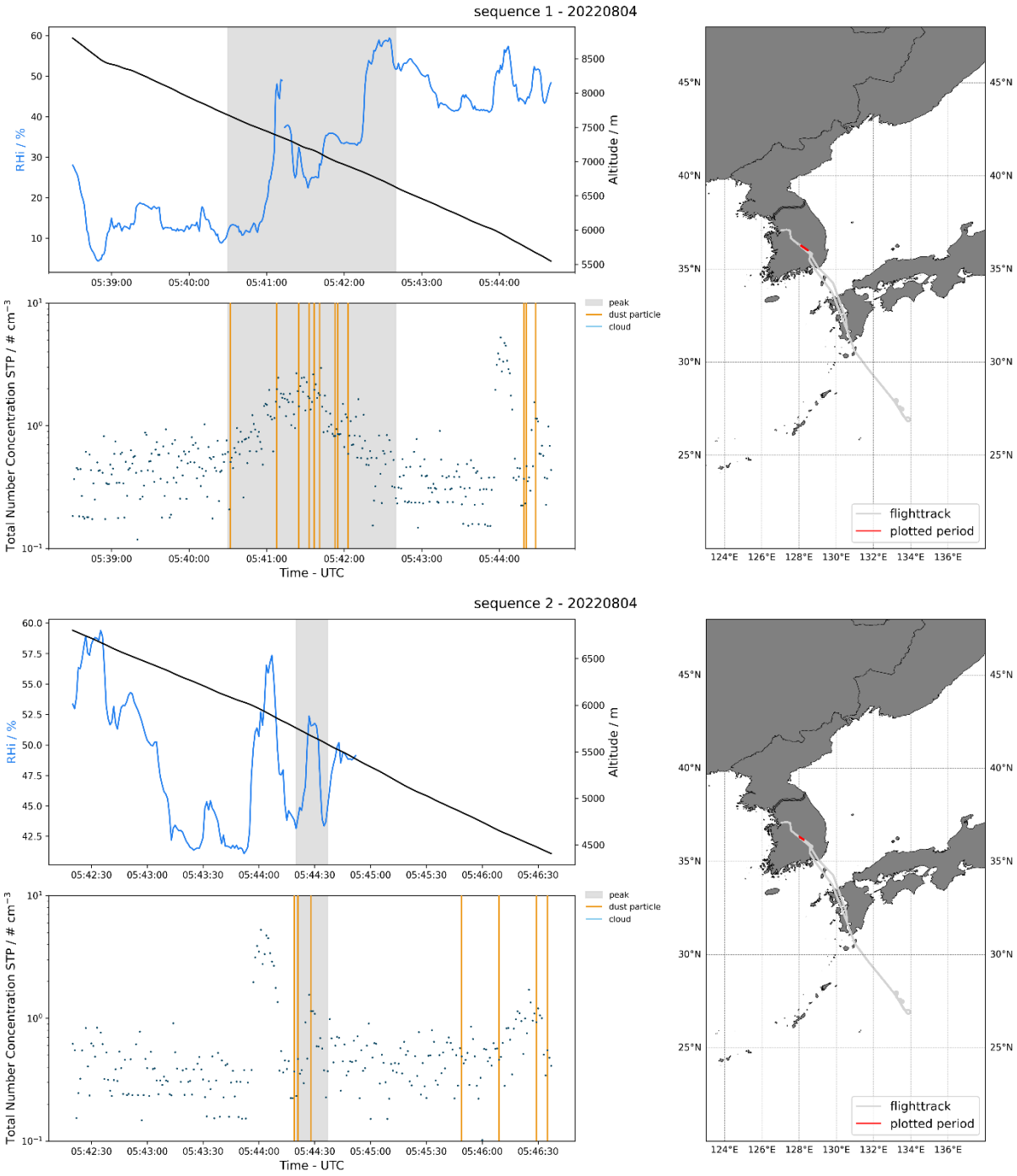

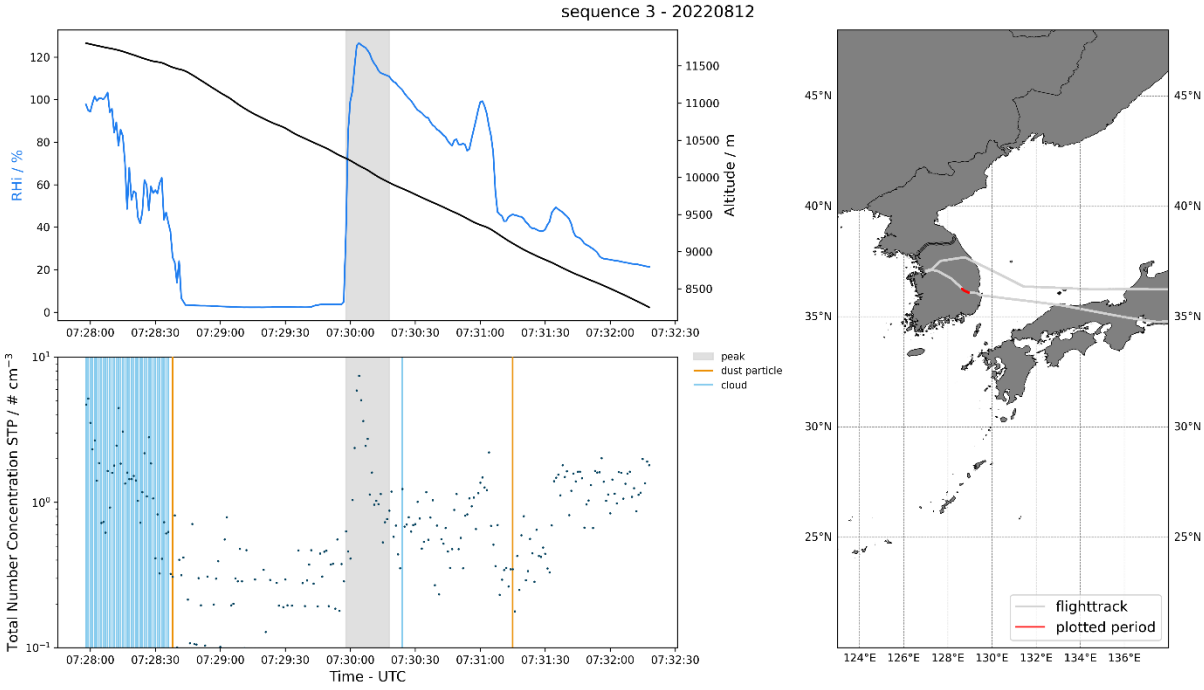
sequence 3 - 20220812
RHi / %
Altitude / m
Total Number Concentration STP / # cm⁻³
peak
dust particle
cloud
Time - UTC
flighttrack
plotted period

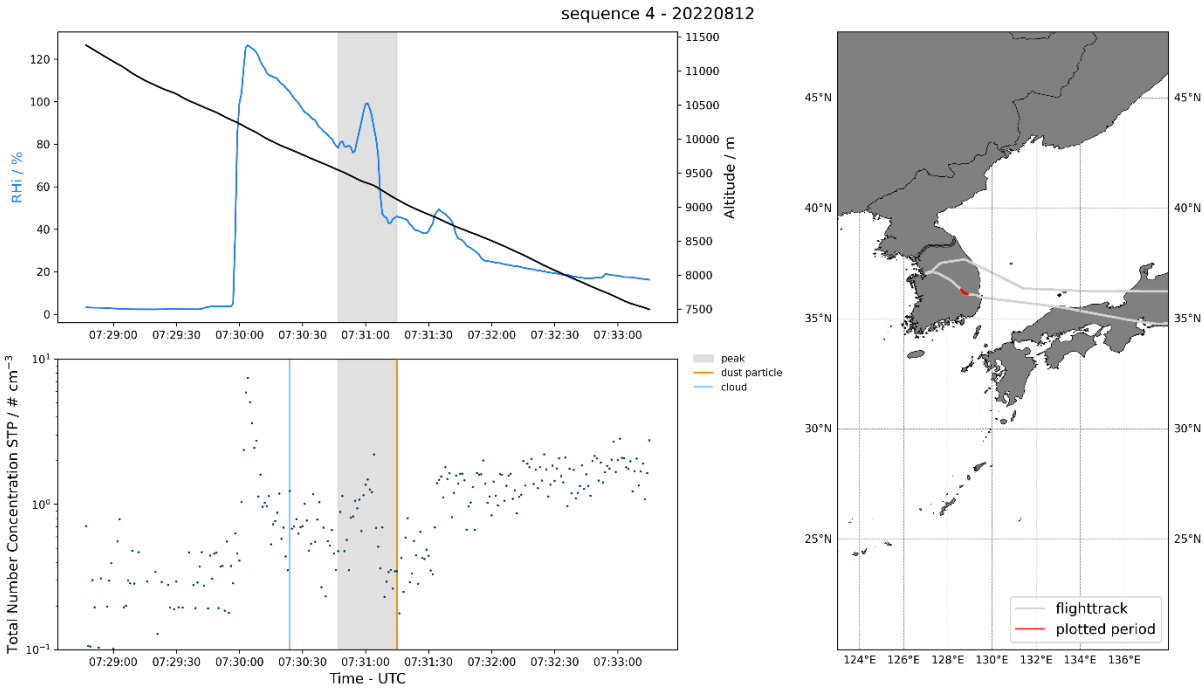
sequence 4 - 20220812
RHi / %
Altitude / m
Total Number Concentration STP / # cm⁻³
peak
dust particle
cloud
Time - UTC
flighttrack
plotted period

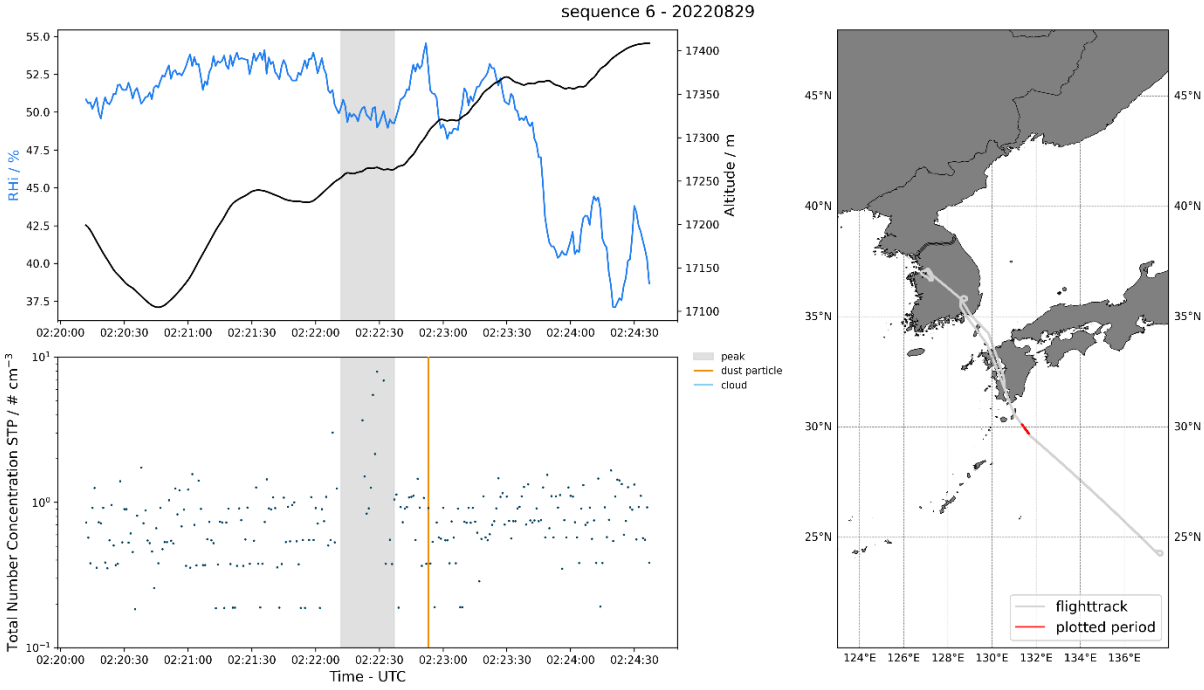
sequence 6 - 20220829
RHi / %
Altitude / m
peak
dust particle
cloud
Total Number Concentration STP / # cm⁻³
Time - UTC
flighttrack
plotted period

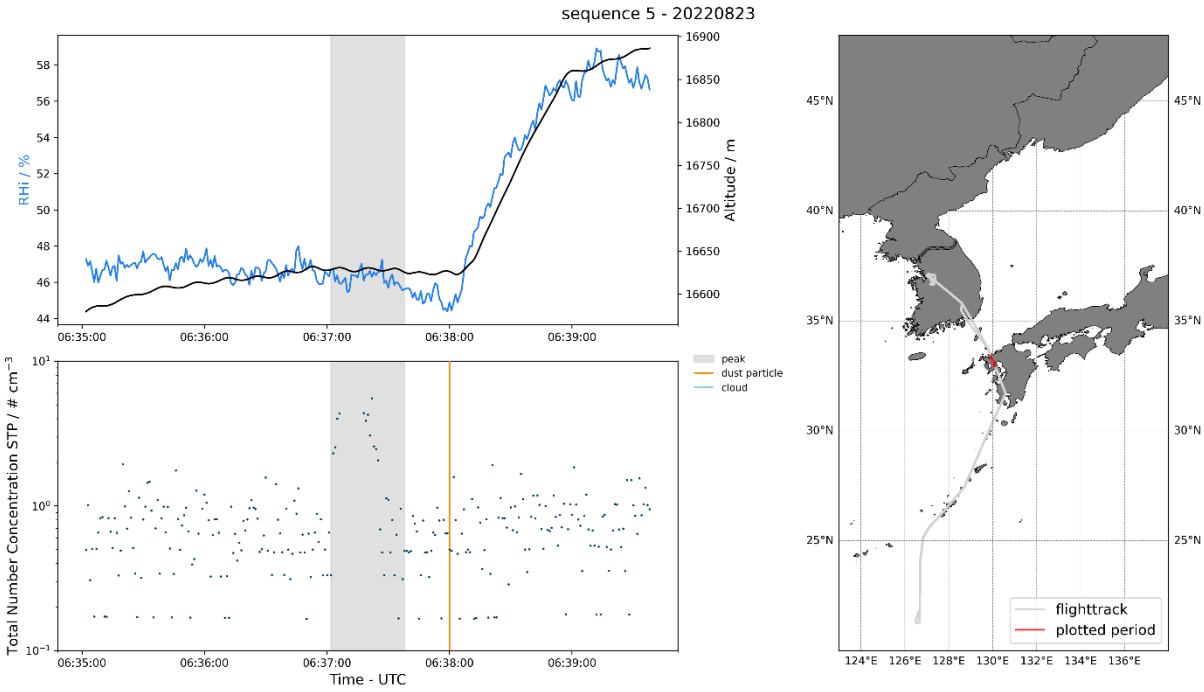
sequence 5 - 20220823
RHi / %
Altitude / m
peak
dust particle
cloud
Total Number Concentration STP / # cm⁻³
Time - UTC
flighttrack
plotted period

C. FLEXPART – Settings of online tool

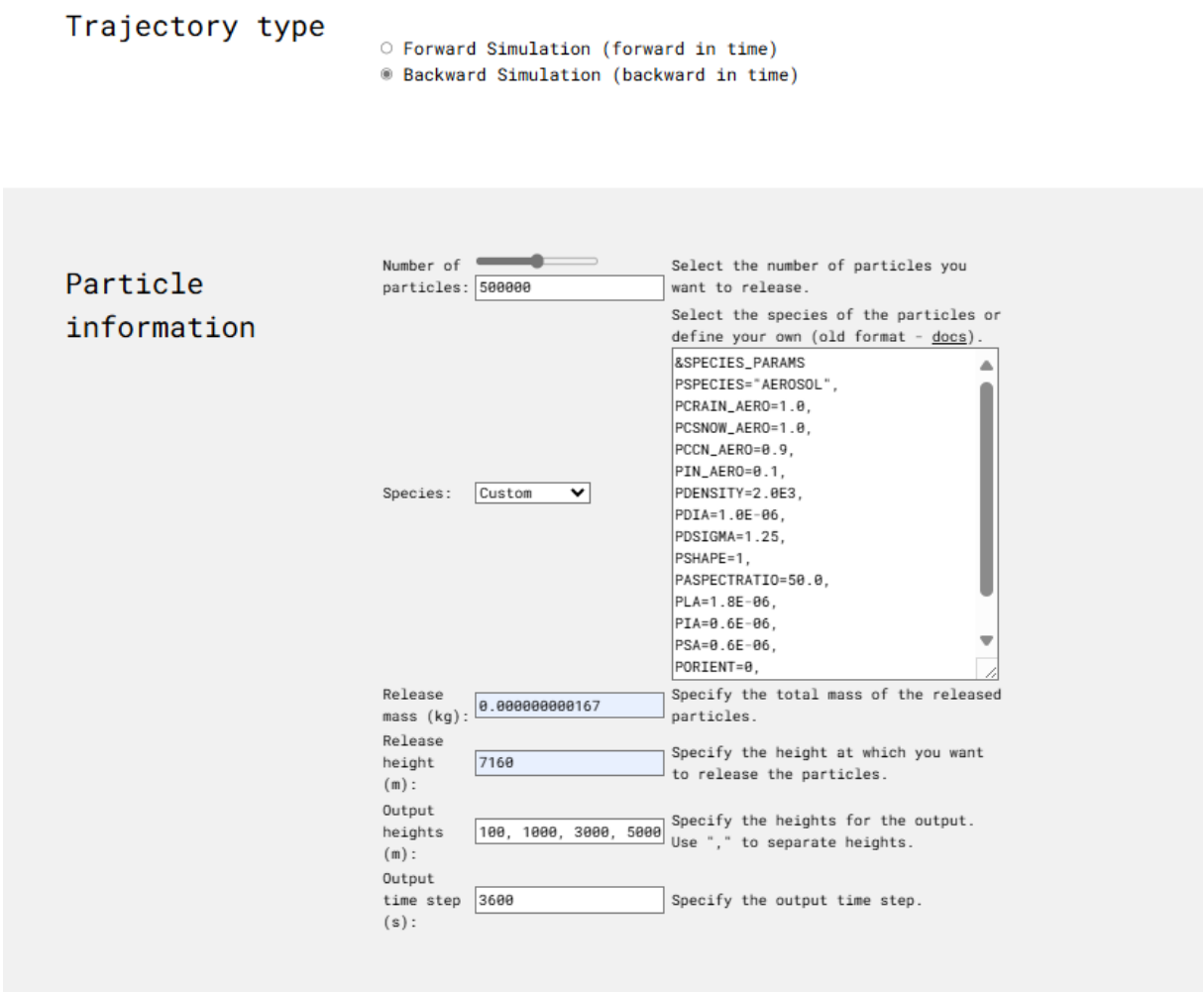

Dates and Times

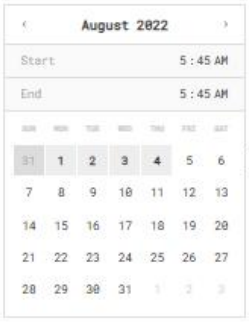

Click to select date and times, maximum of 10 days. 1940 to January 2024.

Source location

Click once to put a marker as source location. Rearrange the output domain to your needs.

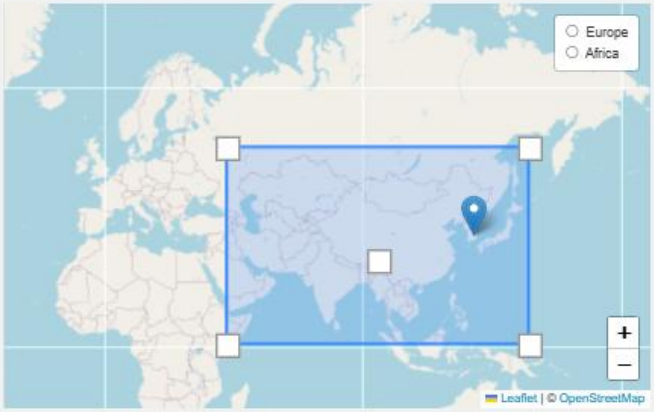

Output grid: 1.0546142 | 42.5392599 | 56.9451540 | 147.6561813

Latitude: 36,1384628 N Longitude: 128,2908730 E

Latitude: N Longitude: W

Deg. Min. Sec. Deg. Min. Sec.

Station, Airport or WMO ID:

Start typing to search for Stations, Countries, WMO Ids.